Temporally Correlated Active Forces Drive Segregation and Enhanced Dynamics in Chromosome Polymers

Sumitabha Brahmachari [1,*], Tomer Markovich [1,2,3], Fred C. MacKintosh,[1,4,5,6] and José N. Onuchic [1,7,5,6]

[1]*Center for Theoretical Biological Physics, Rice University, Houston, Texas 77005, USA*
[2]*School of Mechanical Engineering, Tel Aviv University, Tel Aviv 69978, Israel*
[3]*Chemistry of Living Systems, Tel Aviv University, Tel Aviv 69978, Israel*
[4]*Department of Chemical and Biomolecular Engineering, Rice University, Houston, Texas 77005, USA*
[5]*Department of Physics and Astronomy, Rice University, Houston, Texas 77005, USA*
[6]*Department of Chemistry, Rice University, Houston, Texas 77005, USA*
[7]*Department of Biosciences, Rice University, Houston, Texas 77005, USA*

(Received 5 July 2023; accepted 20 June 2024; published 23 July 2024)

Understanding the mechanisms governing the structure and dynamics of flexible polymers like chromosomes, especially the signatures of motor-driven active processes, is of great interest in genome biology. We study chromosomes as a coarse-grained polymer model where microscopic motor activity is captured via an additive temporally persistent noise. The active steady state is characterized by two parameters: active force, controlling the persistent-noise amplitude, and correlation time, the decay time of active noise. We find that activity drives correlated motion over long distances and a regime of dynamic compaction into a globally collapsed entangled globule. Diminished topological constraints destabilize the entangled globule, and the active segments trapped in the globule move toward the periphery, resulting in an enriched active monomer density near the periphery. We also show that heterogeneous activity leads to the segregation of the highly dynamic species from the less dynamic one, suggesting a role of activity in chromosome compartmental segregation. Adding activity to experimental-data-derived structures, we find active loci may mechanically perturb and switch compartments established via epigenetics-driven passive self-association. The key distinguishing signatures of activity are enhanced apparent diffusivity, exploration of all the dynamic regimes (subdiffusion, effective diffusion, and superdiffusion) at various lag times, and a broadened distribution of observables like the dynamic exponents.

DOI: 10.1103/PRXLife.2.033003

I. INTRODUCTION

Active processes, driven by molecular motors that consume energy (ATP) and exert persistent forces on biopolymers, are ubiquitous and crucial for sustaining cellular life. While motor-driven phenomena such as network contractility [1–3] and motility [4–7] are well studied for stiff cytoskeletal polymer networks, the mechanical consequences of activity remain poorly explored for flexible polymers in the context of genome organization.

Folded chromosomes occupy mutually exclusive territories [8–10], where specific pairs of segments are more likely to be three-dimensional neighbors than others [11–15]. Chromatin bearing distinct epigenetic markers of transcriptional activity (euchromatin and heterochromatin) preferentially interact among themselves, forming A and B compartments [11,16]. A characteristic structural feature is the organization of B compartments inside and A compartments towards the periphery of chromosome territories [9,17,18]. Data-driven effective-equilibrium polymer models, via optimizing the intermonomer-interaction energies, generate ensembles of folded structures consistent with experimental observations such as contact frequencies [18–27]. These models, however, lack a direct connection to physical driving and are insufficient to explore the motor-driven aspects of chromosome structure and dynamics.

Chromosome dynamics is typically subdiffusive at short timescales (seconds), as expected for a polymer [28–31]. However, there is significant heterogeneity in the dynamics of loci, reflected in altered mobility subgroups within the distribution of apparent diffusion constants [32–36]. In the effective-equilibrium approach, the altered mobility has been reasoned to arise from local confinement and/or the local compaction state [33,37]. These structure-centric approaches are limited to only reducing the apparent diffusivity as compared to a free Brownian particle. The possibility of motor-activity-driven enhancement of dynamics is beyond such approaches. It is noteworthy that some chromatin loci have been observed to move superdiffusively at intermediate timescales [35,38,39], which is at odds with any effective-equilibrium or passive approach. Active polymer models with motor-induced persistent forces have indeed shown the

*Contact author: sb95@rice.edu

emergence of superdiffusive dynamics [40–44]. However, active control of chromatin structure is poorly understood.

We propose an active chromosome model where motor-generated forces within a coarse-grained locus contribute to its mobility. Within the active paradigm, coarse-grained motor activity contributes an additive noise that is temporally correlated [see Eq. (1) below]. This contrasts active polymer systems constructed with different temperature particles, where the noise is temporally uncorrelated [45–49]. Active dynamics span subdiffusion, effective diffusion, and superdiffusion. The apparent diffusion of a locus at long lag times is enhanced proportionally to the activity at the locus. Notably, activity not only introduces dynamical heterogeneity, but also affects the chromosome structure. Processes like transcription [50,51], chromatin remodeling [52,53], and loop extrusion [54,55], which rely on ATP-consuming motors and exert forces on chromatin, are the hypothesized sources of activity.

A simplified model of a chromosome as a confined active polymer with soft self-avoidance shows that highly persistent or correlated motor activity typically expands the polymer and increases accumulation at the confinement boundaries. However, if the active kicks are not strong enough to overcome the entanglement constraints presented by chain connectivity and soft repulsion, the highly correlated active kicks lead to a collapsed-globule state stabilized by the polymer entanglements. While the swelling and enrichment of polymer at the boundaries have been observed in active systems with different temperature particles [45,46], the entangled globule is specific to long temporal correlations of the active noise, resembling the motility-induced phase-separated state observed in active colloids [56,57]. Within the presented active model, these biologically relevant structural characteristics are dynamics-driven emergent properties, which we dissect further for mechanistic understanding. On the contrary, in effective-equilibrium models, these structures result from passive potentials like intermonomer interactions [18,19,23–26,58–60]. Interestingly, information on the steady-state structure alone cannot distinguish between active and passive models. The active steady-state polymer conformations may look identical to the passive ones of a completely unrelated system. For example, the collapsed globule of a purely self-avoiding active polymer may be structurally disguised as a passive polymer with strong intermonomer attractions. This highlights a potential ambiguity in deciphering the underlying mechanism from structural ensembles alone. However, signatures of enhanced dynamics, such as superdiffusion or high apparent diffusivity, and correlated motion over long spatiotemporal scales unambiguously point towards an active system. While passive physical potentials have successfully recapitulated structures of chromosome compartments [18,19,23–26,60], the presented model suggests that persistent motorized forces are a source of dynamic regulation of compartmentalization. We hope this work will lead to new experiments investigating the motor-driven dynamic aspects of chromosome compartments.

The layout of the article is as follows. We first describe the active polymer model (Fig. 1) and then investigate the steady state of a confined active homopolymer (Fig. 2). We explain the mechanisms of active regulation of the active structure and dynamics. To understand the consequences of heterogeneous activity, we simulate an active-passive block copolymer, uncovering features such as phase segregation of active and passive monomers (Fig. 3). Building upon the intuition from the homopolymer and the block copolymer models, we discuss the model's relevance to chromosomes. By adding active loci to a passive chromosome model (MiChroM [19,61]), we explore active perturbation to the effective-equilibrium structures (Fig. 4). Finally, we conclude with an overview and discussion.

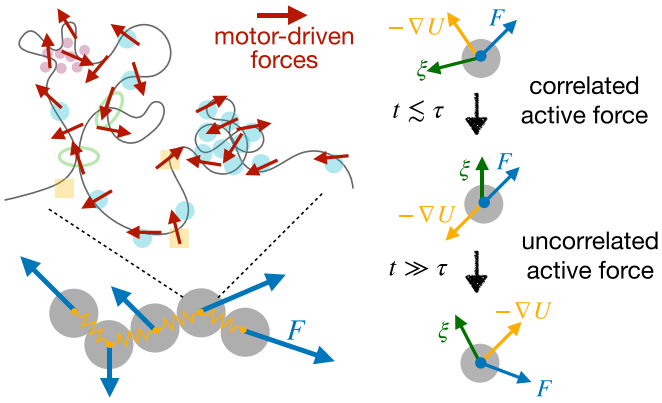

FIG. 1. Schematic active polymer model. Microscopic motors exerting forces on the polymer are depicted as small red arrows. Each coarse-grained monomer containing distributed point forces experiences an active noise with amplitude F such that the net active force on the polymer vanishes. At each time step, every monomer experiences three kinds of forces [Eq. (1)]: temporally uncorrelated thermal noise ξ, passive forces derived from the polymer potential $-\nabla U$, and the active force F. The active kicks are correlated over a timescale τ, the correlation time. When averaged over long lag times $t \gg \tau$, the correlation of the active kicks vanishes [Eq. (2)].

II. ACTIVE POLYMER MODEL

The active polymer model hypothesizes the activity of molecular motors as point forces [41,43,44,62–66]. As these are internally generated and not external body forces, they must be balanced, with no net force. We ensure this in our coarse-grained model with multiple active point forces that are randomly oriented (Fig. 1) and average to zero both on larger network scales and when averaged over long times. However, the motor binding kinetics makes the active force correlated over short timescales, set by the motor-residence time. This results in noiselike active kicks that are temporally correlated. The temporal decay of correlations is determined by the distribution of residence times of the motors. If motor (un)binding events are independent, the residence times follow a Poisson distribution, giving an exponentially correlated noise. Following previous approaches [41,43,64,66,67], we assume that the active force correlation decays exponentially, characterized by a single timescale τ, the correlation time.

The overdamped equation of motion of the nth active monomer in a thermal bath at temperature T reads

$$\gamma \frac{dr_n}{dt} = -\nabla_n U + \xi_n(t) + f_n(t). \tag{1}$$

Here γ is the drag coefficient and $-\nabla_n U$ represents the passive forces derived from the polymer potential, like the harmonic bonds between nearest neighbors. Random forces from thermal fluctuations, represented by ξ_n, are uncorrelated: $\langle \xi_n(t)\xi_m(t')\rangle = 2\gamma k_B T\delta(t-t')\delta_{mn}$, where k_B is the Boltzmann constant. The active noise f_n, unlike thermal fluctuations, is correlated:

$$\langle f_n(t) f_m(t')\rangle = F^2 \exp(-|t-t'|/\tau)\delta_{mn}. \tag{2}$$

The amplitude of active noise F, a free parameter in the model, is expected to scale with the number of motors within the monomer. Note that we assume that the active forces of the neighboring coarse-grained monomers are uncorrelated. We ignore explicit correlations of the active force along the coarse-grained polymer contour, which may be of biological interest [48] and is left for future work. Including the effect of torque-inducing motors is yet another biologically relevant future possibility [68].

The technique of representing activity as a correlated noise has been discussed both in the context of motor activity in the cytoskeleton [62,64,67,69,70] and for active colloidal solutions, where the term active Ornstein-Uhlenbeck particles (AOUPs) is used [57,71]. The steady state of AOUPs shows remarkable features such as inhomogeneous density profiles in confinement and motility-induced phase separation (MIPS): Self-avoiding AOUPs segregate into a dense phase, mimicking effective attractive interactions [56]. The AOUP model has also been adopted to study active Rouse polymers [41,43,72]. These polymer models focus on dynamics, while structural features, such as the analog of MIPS, remain largely unexplored.

Mean persistent path and active steady state

The steady state of the active polymer is governed by a competition between the active (F and τ) and passive (T) parameters. A metric of activity is the emergent length $\lambda_a \equiv F\tau/\gamma$, which we call the *mean persistent path* of an active monomer. This is the average distance an active monomer moves persistently before changing direction. In the presence of thermal fluctuations of strength T, the active features dominate only when the active temperaturelike quantity $\theta_a = F\lambda_a$ is dominant: $\theta_a > T$. We generally refer to the parameter regime with $\theta_a > T$ as the active steady state and $\theta_a < T$ as the thermal-dominated passivelike steady state [Figs. 2(a) and 3(b)].

III. RESULTS

A. Self-avoiding active homopolymer in confinement

The physics underlying the active model [Eq. (1)] has been explored in the context of Rouse chains [41,43,72], which is in agreement with our model (see Appendix B and Fig. 5). Here we study the behavior of an active homopolymer with biologically relevant constraints: self-avoidance and confinement (see Appendix A for details of the potentials). Figure 2 shows the results for a self-avoiding polymer with $N = 2000$ monomers that is confined within a sphere of radius $R_c = 16\sigma$ such that the volume fraction $\phi \equiv N\sigma^3/(2R_c)^3 \approx 6\%$ is in the physiological regime for confined chromatin [73]. Since we simulate a single chromosome polymer, the confinement effectively mimics the confines of the chromosome territory. Here σ is the monomer diameter used as a unit of distance, the unit of energy is ϵ, and the unit of time is $\tau_{\rm sim}$ (see Appendix B for details).

1. Activity drives dynamic compaction in self-avoiding polymers

A prominent signature of the active steady state is the compaction of a self-avoiding polymer into a denser globule with a lower radius of gyration than the passive case [Fig. 2(a)]. The compact state emerges when the mean persistent path λ_a exceeds the average spacing between monomers, given by the concentration-dependent distance $\lambda_{\rm coll} \approx \sigma/\phi^{1/3}$. In this regime ($\lambda_a > \lambda_{\rm coll}$), active monomers, even after colliding with each other, maintain their active noise direction, resulting in them getting trapped in a dynamically driven dense state. The compact state is characterized by dense clusters that coexist with less dense regions, where the correlation time dictates the stability of the compact clusters.

2. Activity correlated over long times establishes a collapsed entangled globule

Activity with a long correlation time traps the polymer into a globally collapsed globule [Fig. 2(a)]. The collapsed globule is stabilized by topological entanglements, making the globule a long-lived state. Topological or polymer entanglements refer to the hindrance of the polymer segments to pass through each other due to the combined effect of the soft self-avoidance between monomers and the polymer connectivity. The polymer segments on the periphery of the globule may reorient their average active noise direction to escape the collapsed state. This leads to some segments coexisting in a less dense state with the entangled collapsed globule [Fig. 2(d)]. Such segments, however, after momentarily exploring the less dense space outside the globule, reencounter the dense state, thus keeping the globule from dissociating. The compact structures driven by activity are liquidlike; however, the entangled globule exhibits an enhanced solidlike packing and mechanical integrity [Fig. 2(c)]. The collapsed-globule state is destabilized when the active force amplitude is smaller than the thermal fluctuations $F < k_B T/\sigma$, since thermal fluctuations destroy the correlated motion driving this state.

The collapsed globule is reminiscent of the segregated state in active colloids exhibiting MIPS [56,57]. The collapsed state occurs at a lower density in active polymers ($\phi \sim 0.05$) compared to AOUPs ($\phi \sim 0.5$) [57,74]. This stems from polymer entanglements stabilizing the dense phase. Enhancement of active signatures for polymers compared to colloids with the same activity has been observed in simulations [46]. Semiflexible polymers without self-avoidance show activity-driven compaction because activity enhances transverse fluctuations that lead to a lower end-to-end distance [75]. However, this compaction mechanism differs from the self-avoidance and polymer connectivity-driven collapse into the entangled globule.

3. Large active noise amplitudes destabilize the collapsed globule via stretching bonds and reducing entanglements

The collapsed entangled globule gradually disappears as the active noise amplitude F is increased [Fig. 2(a)].

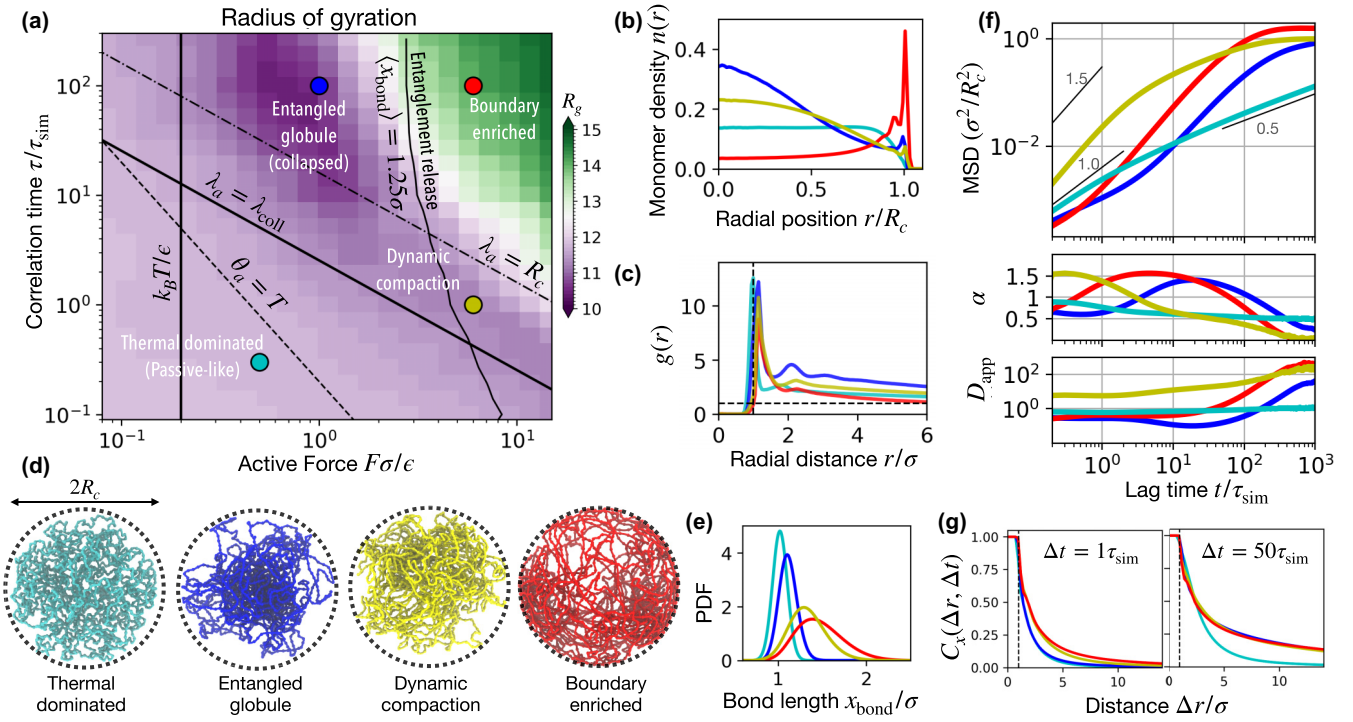

FIG. 2. Self-avoiding active polymer in spherical confinement. (a) Active regime diagram spanned by the active force F (ϵ/σ units) and the correlation time τ ($\tau_{\rm sim}$ units). The colors depict the radius of gyration R_g of the polymer (σ units). The active steady state ($\theta_a > T$) shows compaction when the mean persistent path $\lambda_a \equiv F\tau/\gamma$ is longer than the mean collision distance between the monomers $\lambda_{\rm coll} = \sigma/\phi^{1/3}$, where ϕ is the confinement volume fraction. This compaction is characterized by short-lived (dynamic) locally collapsed clusters. Long correlation times lead to a globally collapsed, entangled-globule state. When λ_a is greater than the confinement dimension R_c, the monomers have a tendency to get trapped at the boundary wall. However, release of entanglements is necessary to destabilize the competing entangled-globule state in order to enrich the boundaries. Hence, only when the bonds are stretched by the active force (mean bond distance $\langle x_{\rm bond}\rangle > 1.25\sigma$), leading to entanglement release, does the boundary-enriched state appear. Representative parameter sets for the four regimes are shown in colored circles for which various observables are plotted: thermal dominated ($F = 0.5$, $\tau = 0.3$, cyan), entangled globule ($F = 1$, $\tau = 100$, blue), dynamic compaction ($F = 6$, $\tau = 1$, yellow), and boundary enriched ($F = 6$, $\tau = 100$, red). We used $k_BT = 0.2\epsilon$ for all simulations. (b) Radial profile of the monomer number density $n(r)$. (c) Radial distribution function $g(r)$ showing a peak at 1σ corresponding to self-avoidance. Only the entangled-globule state shows prominent successive peaks reflecting the collapsed state and an increased solidlike behavior. (d) Representative simulation snapshots, where the dotted line represents the spherical confinement with radius R_c. Note that the collapsed structures may appear as a passive polymer with self-adhesion, while the boundary-enriched state might resemble a passive polymer with boundary adhesion. This refers to the ambiguity in deciphering the underlying mechanism from structural ensembles alone. (e) Bond length distribution showing the increase in the mean bond length $\langle x_{\rm bond}\rangle$ for higher active force F. (f) Mean-square displacement (MSD), normalized by the confinement dimensions, versus lag time t ($\tau_{\rm sim}$ units), where the scaling exponents 0.5, 1.0, and 1.5 are drawn for comparison. The dynamic exponent α and the apparent diffusivity $D_{\rm app}$ are plotted in the subpanels below. Active steady states span subdiffusion, effective diffusion, and superdiffusion. The exponent α goes to zero at long lag times due to the confinement-induced saturation of MSD. (g) Correlation of monomer displacements measured over Δt, plotted as a function of the distance between the monomers Δr. Active steady states show enhanced correlated motion.

Increasing the active force F increases the fraction of the polymer that coexists in the less dense space outside the globule, eventually leading to the complete destabilization of the dense state. This destabilization is due to the stretching of the bonds of the polymer by strong active kicks, which diminishes the topological constraints. Two non-neighboring segments with stretched bonds are more likely to pass through each other than get trapped in a dense state. We find that an approximately 25% increase in the average bond length is enough to destabilize the collapsed state [Figs. 2(a) and 2(e)].

Following our rationale, increasing the bond stiffness, which decreases the bond length and reinforces the entanglement constraints, stabilizes the collapsed state for higher active noise amplitudes (Fig. 6). The stability of the entangled-globule state for low active noise amplitudes is governed by the thermal temperature. When $F < k_BT/\sigma$, uncorrelated thermal noise dominates the correlated active noise, leading to destabilization of the collapsed entangled state [Figs. 2(a) and 7]. Note that, although, the thermal noise domination makes the structure appear equilibriumlike, the dynamics at long correlation times can still show signatures of activity.

4. Competition between mean persistent path and confinement dimension leads to boundary enriched polymer

A boundary-enriched state emerges for high active force and high correlation times, where the monomer density peaks

at the boundary and is depleted at the center, and the polymer is expanded such that the radius of gyration assumes the size of the box [Figs. 2(a) and 2(b)]. When the mean persistent path is longer than the confinement dimension, i.e., $\lambda_a > R_c$, the active monomers collapse on the boundary wall. The active monomers with long correlation times keep pushing against the wall, while upon reorientation of their active force direction, they move in a correlated fashion until encountering the other side of the boundary. However, this state only appears when the entanglement-driven constraints are sufficiently weaker so that the polymer does not get trapped in the entangled-globule state. Hence, the two criteria for the appearance of this state are the high force, necessary for the release of entanglements, and a high enough mean persistent path, necessary for getting trapped at the boundary [Fig. 2(a)].

Boundary enrichment comes about from a competition between monomer activity and confinement; hence, self-avoidance and polymer connectivity are not necessary for establishing this state. As a result, active Rouse chains and active gas or colloidal particles (AOUPs) both exhibit the emergence of boundary enrichment with the appropriate mean persistent path (Figs. 8 and 9).

5. Structural ensembles are insufficient to distinguish between effective-equilibrium and actively driven phenomena

The conformations of the active steady state may appear to belong to a completely unrelated passive system. For example, the collapsed state might look like a polymer with self-adhesive interactions [Fig. 2(d)] or the boundary-enriched structures may appear as though the monomers have attractive interactions with the confinement wall [Fig. 2(d)]. This clearly suggests that structural ensembles are not enough to distinguish between the underlying active and passive mechanisms. However, the dynamics may hold key distinguishing features.

6. Regimes of polymer dynamics

The dynamics in viscoelastic media is often characterized by anomalous diffusion, with the mean-square displacement (MSD) given by $\langle [r_n(s+t) - r_n(s)]^2 \rangle = Dt^\alpha$, where the dynamical exponent of the lag time t classifies distinct dynamic regimes: diffusion for $\alpha = 1$, subdiffusion for $\alpha < 1$, and superdiffusion for $\alpha > 1$. The coefficient D is an apparent diffusivity parameter. A free passive particle executes diffusion, where D is the diffusion constant proportional to the thermal temperature: $D_{\text{free}} = k_B T/\gamma$.

Polymer relaxation spans multiple timescales that arise because fluctuations with longer wavelengths decay slower. The shortest wavelength fluctuations, corresponding to bond fluctuations, relax at short timescales $\tau_{\text{bond}} \sim \gamma/k$, where k is the bond stiffness. On the other end of the spectrum, $\tau_{\text{Rse}} \approx N^2\gamma/k\pi^2$ corresponds to the relaxation time of the longest wavelength [76] (see Appendix B; for Figs. 2 and 3, $\tau_{\text{bond}} \approx 0.1\tau_{\text{sim}}$ and $\tau_{\text{Rse}} \approx 10^4\tau_{\text{sim}}$). The third important timescale is the active correlation time τ. An interplay of these timescales determines the dynamic signatures.

For lag times shorter than the bond relaxation time ($t \ll \tau_{\text{bond}} < \tau$), passive polymer dynamics resembles free-particle diffusion [Fig. 2(f)]. For lag times larger than the bond relaxation but smaller than the longest polymer relaxation time ($\tau_{\text{bond}} < t < \tau_{\text{Rse}}$), passive dynamics exhibits subdiffusion ($\alpha < 1$) [Fig. 2(f)] [76]. This originates from each monomer having to drag a portion of the chain with it. Within this regime, active polymers may have substantially different signatures [Figs. 2(f), 3(f), and 5]. At lag times longer than τ_{Rse}, passive motion returns to diffusion, corresponding to the polymer center-of-mass motion [76]. For chromosomes, τ_{Rse} is typically very long and experimentally inaccessible. For this reason, we have not included this regime in Figs. 2(f) and 3(f). In the case of confined polymers, this may not be observed because MSD at such long lag times may be saturated due to the confinement. The dynamic regimes of the active self-avoiding polymer are similar to that of the active Rouse chain (see Appendix B and Fig. 5) [41,43], since all the dynamic signatures originate from a competition between the monomer activity and the nearest-neighbor bonds in the polymer potential.

7. Superdiffusion in active polymers

The leading-order active contribution to MSD scales as quadratic in time, approximately $(t/\tau)^2$, driving a superdiffusive regime [41,43] (Appendix B), whereas at the short timescales $t \ll \tau_{\text{bond}}$, the thermal contribution is linear in lag time. This results in the MSD asymptotically approaching the diffusive (linear) regime near zero lag times irrespective of activity [Fig. 2(f)].

The activity-driven superdiffusion in the MSD curves appears when the approximately t^2 active contribution exceeds the passive forces. The dominance of the active forces leads to a superdiffusive exponent when the lag time is comparable to the correlation time [Fig. 2(f)]. For short correlation times $\tau \approx \tau_{\text{bond}}$, the active polymer shows superdiffusion at the timescales of free-monomer dynamics [Fig. 2(f)].

For correlation times that are longer than the bond relaxation time ($\tau_{\text{bond}} < \tau < \tau_{\text{Rse}}$), the dynamics show a subdiffusive regime at intermediate lag times $\tau_{\text{bond}} < t < \tau$ [Fig. 2(f)]. This subdiffusion is a result of compensation of the persistent active drive by the polymer potential [41]. Interestingly, the entangled globule shows an extended subdiffusive regime due to the suppression of dynamics in a crowded environment [Fig. 2(f)].

Active polymer dynamics restores to subdiffusion at lag times longer than the correlation time [Fig. 2(f)]. Within our model, at these long lag times, the active noise becomes indistinguishable in its time dependence from thermal noise. However, the motion is enhanced in amplitude due to the active noise contribution, reflected in an increased apparent diffusivity.

8. Activity typically enhances the apparent diffusivity

We compute an apparent diffusivity from the simulated MSD curves: $D_{\text{app}} \equiv \text{MSD}/t^\alpha$, where the exponent $\alpha \equiv \partial(\ln \text{MSD})/\partial(\ln t)$. Note that the apparent diffusivity is a lag-time-dependent coefficient that is equal to the diffusion constant when $\alpha = 1$. For lag times shorter than the bond relaxation time τ_{bond}, the apparent diffusivity for a passive polymer is set by the free-particle diffusion constant $D_{\text{app}} \approx k_B T/\gamma$ [Fig. 2(f)], while at lag times longer than the polymer relaxation time $t > \tau_{\text{Rse}} > \tau$, the passive apparent diffusivity

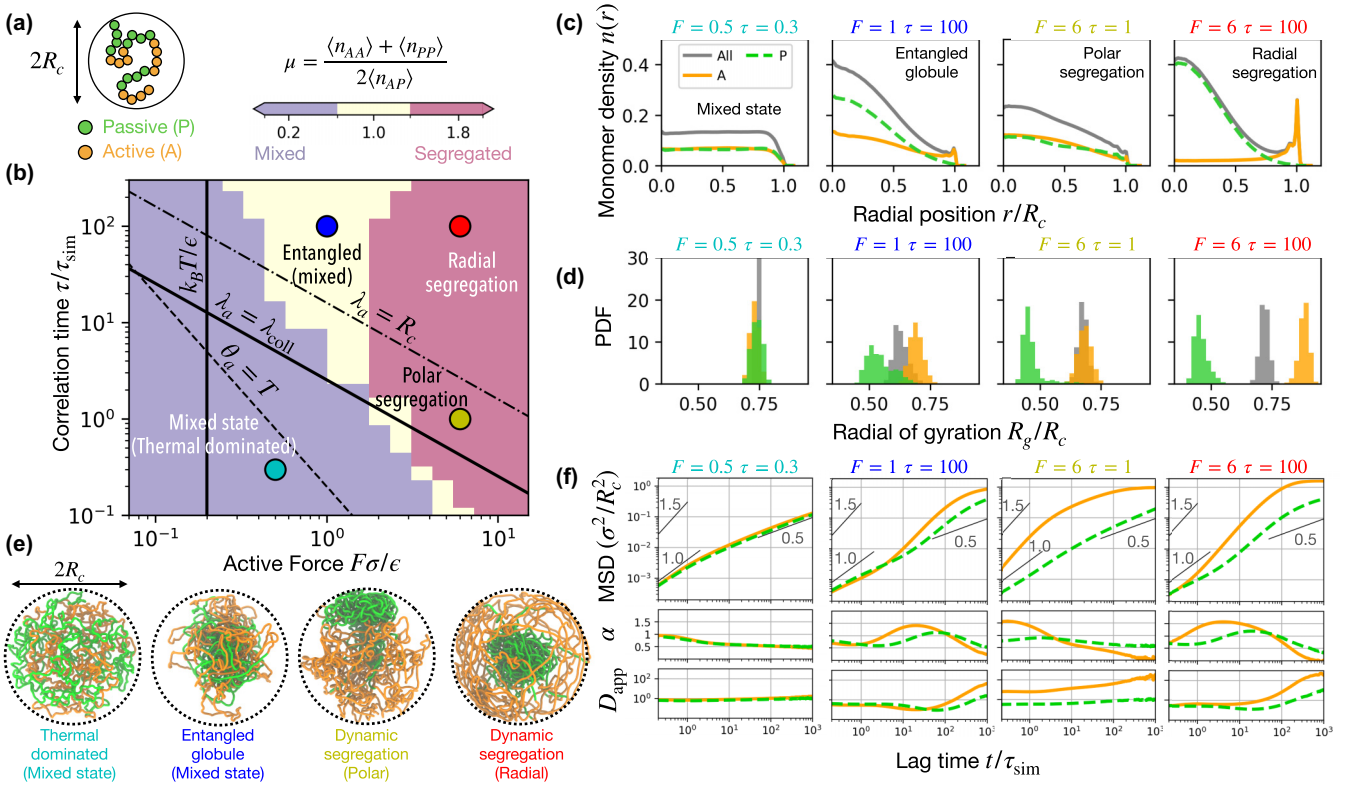

FIG. 3. Phase separation of active and passive blocks of a confined self-avoiding polymer. (a) Schematic of the confined block copolymer with active (A) and passive (P) blocks with orange and green colors, respectively. (b) Active regime diagram, where colors represent the phase-separation coefficient μ, defined as the abundance of homotypic (A-A and P-P) over heterotypic (A-P) contacts. When $\mu > 1$ (pink), there is segregation of the A and P blocks, while $\mu < 1$ (purple) signifies a mixed state. The active steady state generally shows a tendency to segregate the active and passive blocks due their altered dynamics. However, the entangled-globule state is only marginally segregated due to topological constraints. Given the active force is strong enough to release entanglements, activity with $\lambda_a > R_c$ segregates the active and passive blocks radially. Otherwise, the passive blocks are segregated to a pole of the confinement. The four colored circles depict parameter sets for the four distinct regimes: thermal dominated ($F = 0.5$, $\tau = 0.3$, cyan), entangled globule ($F = 1$, $\tau = 100$, blue), polar segregation ($F = 6$, $\tau = 1$, yellow), and radial segregation ($F = 6$, $\tau = 100$, red). We used $k_BT = 0.2\epsilon$ for all simulations. (c) Radial profile of monomer density $n(r)$ for active (orange, solid lines), passive (green dashed lines), and all monomers (gray solid lines). (d) Radius of gyration of the active (orange), passive (green), and all monomers (gray). (e) Representative simulation snapshots with A and P monomers colored in orange and green, respectively. (f) Mean-square displacement, the dynamic exponent α, and apparent diffusivity D_{app} versus lag time, for active and passive monomers corresponding to the four regimes. The dynamics of the active monomers are the same as described before [Fig. 2(c)]. The passive monomers deviate from a purely passive behavior due to their polymer connectivity with the highly dynamic active monomers.

is again a constant $D_{app} \approx k_BT/N\gamma$ and is lower due to the center-of-mass motion [76].

The apparent diffusivity for active polymers shows enhancement over the corresponding passive behavior only for lag times longer than the correlation time [Fig. 2(f)]. Interestingly, the active apparent diffusivity may also show suppression, such as in the entangled-globule state. Competition between the active noise and the passive polymer potential underlies this suppression.

While superdiffusion is a unique characteristic of the active steady state, investigating the dynamics at the appropriate lag time is essential to observe this. When lag times are longer than the active correlation time, the dynamics appear passive with a higher effective temperature [Fig. 2(f)], while lag times smaller than the correlation time may show suppressed dynamics akin to lower effective temperatures. Hence, observations of passivelike dynamic exponents do not rule out active forces; the apparent diffusivity and MSD exponents should be scrutinized at various lag times to investigate an active component.

Active dynamics bear another key signature: correlated motion of the monomers over long distances. Activity-driven compact clusters exhibit correlated motion, reflected in a shallower decay of the two-point displacement correlation function for the active steady states [Fig. 2(g)].

B. Phase segregation of active and passive blocks of a confined self-avoiding polymer

To explore the effect of heterogeneity in activity along a polymer, we study a block copolymer with alternating active (A) and passive (P) blocks [Fig. 3(a)]. The polymer has $N = 2000$ monomers and each alternating active and passive block of size $n = 200$ monomers. We use the same self-avoidance and confinement conditions ($\phi = 0.06$) as before (see Appendix A). In the passivelike regime ($T > \theta_a$), the

A and P blocks mix due to entropy and the dynamics is equilibriumlike [Fig. 3(f)]. The active steady states ($T < \theta_a$) tend to show phase segregation of A and P blocks. Spatial separation of two species with different dynamics underlies this segregation. Highly dynamic active monomers occupy a larger share of the confinement volume, relegating the passive monomers into a compact segregated state. Interestingly, the spatial organization of the segregated phases is governed by active correlation time [Figs. 3(b), 3(c), and 3(e)].

Activity-driven phase separation between the active and passive blocks is observed only when the active force is large enough to release entanglements [Fig. 3(b)]. Phase separation is measured via the coefficient μ, defined as the ratio of homotypic to heterotypic pairwise contacts between interblock monomers. A pairwise contact is defined when the intermonomer distance is less than 1.5σ (Appendix A). When $\mu > 1$ the active and passive blocks segregate, whereas $\mu < 1$ denotes the mixed state.

The entangled-globule state shows an overall collapse of the entire polymer, where the active and passive blocks are not well segregated [Figs. 3(b)–3(e)]. The regime corresponding to boundary enrichment of the active blocks (high F and high τ) shows strong phase separation [Figs. 3(b) and 3(c)]. In this regime, the passive blocks are highly compacted and reside at the center, while the active blocks spread over the boundary wall [Fig. 3(e)]. Phase separation is also observed in the regime of low mean persistent path (high F and low τ). This state is characterized by compact passive domains and expanded, highly dynamic active blocks that are segregated, without any radial preference, in a polar fashion [Figs. 3(b)–3(e)]. Increasing the thermal temperature releases entanglements for passive blocks and leads to a boundary enrichment of passive monomers (Fig. 10).

The dynamics of the active monomers in the block copolymer basically resemble the regimes explored in the active homopolymer case [Figs. 2(f) and 3(f)]. Interestingly, the dynamics of the passive blocks show deviation from passive behavior [Fig. 3(f)]. The bonded interactions with the active monomers make the passive blocks more dynamic.

Phase separation of passive block copolymers is typically modeled using the Flory-Huggins approach, where blocks are assigned self- and mutual interactions. The active phase separation presented here is fundamentally different, as it is dynamically driven. Mutually repulsive active monomers segregate from the passive monomers, creating regions of high and low dynamics. Although the structural ensembles of a Flory-Huggins polymer may appear similar to the active phase segregated system, the dynamics are more heterogeneous and span multiple regimes for the activity-driven structures. The dynamic segregation within an active-passive mixture has been observed in other polymer models [47,77].

C. Implications for chromosomes

Chromosomes are active matter, where motorized processes like transcription, loop extrusion, and chromatin remodeling are continually driving the structure and dynamics. Our understanding of chromosome folding and the underlying mechanics has been consolidated due to the emulsification of experimental data such as Hi-C contact maps [11–13] and polymer models [18–27]. However, the existing chromosome models are predominantly effective-equilibrium approaches, lacking direct signatures of activity such as superdiffusive chromatin loci [35,38,39].

Here we use the presented active model to study chromosomes. The amplitude of the active noise is set by the typical stretching elasticity of chromatin: $F \approx 1$–10 pN [78,79]. The active correlation time τ is a measure of the motor-residence time. While chromatin remodelers typically show fast, subsecond dynamics [53], persistent bursts of gene activity, corresponding to RNA polymerases moving processively, may last for many minutes [80]. Loop extruding enzymes structural maintenance of chromosomes (SMC) complexes typically extrude a 50 kb DNA loop in tens of seconds [55]. Note that extrusion activity of loops shorter than a monomer size (approximately 50 kb) may be considered within this approach, whereas large loops spanning multiple monomers should be incorporated explicitly as large force dipoles. Hence, we argue that the physiological range for the correlation time is $\tau \approx 1$–10^2 s, where the higher (lower) end of the spectrum is associated with transcription (chromatin remodeling and extrusion of short loops). Consequently, at experimentally realizable timescales (1–100 s), we expect chromatin regions housing highly transcribed genes to show superdiffusive signatures, whereas loci containing loop extruders or chromatin remodelers are expected to show subdiffusion with an enhanced apparent diffusivity.

The eukaryotic genome is typically confined within the nucleus with a volume fraction approximately 1%–10% [73]. The hierarchical organization of the genome may introduce effective confinement with a similar volume fraction but at a smaller dimension. For example, the chromosome territories, which are about an order of magnitude smaller than the nuclear dimension, may effectively confine chromosomal loci, like genes or centromeres [10]. Hence there are multiple confinement length scales that may compete with the mean persistent path of an active chromosome locus.

1. Activity-driven phase separation as a mechanism of chromosome compartmentalization

Compartmentalization is an important feature of chromosome folding in the interphase chromosomes of eukarya [11,13,16]. Compartments are globules formed by colocalization of sequentially distant genomic elements, reflected in the off-diagonal plaidlike patterns of the Hi-C maps. Hi-C-defined (sub)compartments are structural classes obtained via dimensionality reduction, e.g., principal component analysis of the pairwise genomic-interaction patterns [11,13]. These compartments are correlated to the cellular gene expression profile and show tissue- or cell-type-specific variability [12,81–83]. However, the mechanics governing the relationship between structurally annotated compartments and gene expression is not understood.

The active model suggests phase-segregated structures, akin to A/B compartmentalization, may arise from altered activity between A and B segments. The distinguishing characteristics of active compartments are their enhanced dynamics, elevated apparent diffusivities, and the possibility of a superdiffusive dynamic regime [Figs. 2(c)–2(e) and

3(f)]. Polymer-entanglement-based constraints stabilize these motor-driven compartments. Hence, increased activity of enzymes like type-II DNA topoisomerase, releasing topological constraints, is expected to destabilize these compartments.

A passive mechanism for compartmentalization, which has been widely explored, is short-range attractive interactions originating from the chromatin loci's chemical nature (epigenetics) [18–27,60]. Globules established via motor activity may act as a nucleation site for the three-dimensional spreading of epigenetic marks [84,85]. This will lead to robust compartments that persist even when the motor activity ceases. Alternately, compartments established via passive attraction may be disrupted or perturbed by altered activity.

To investigate how passive compartments may respond to activity, such as increased transcription, we simulate active loci within the passive MiChroM model [19,61]. Briefly, the optimized MiChroM potential contains favorable interactions that may be divided into two categories: first, the phase-separation term that drives compartmentalization, and second, the ideal chromosome term that drives lengthwise compaction [19,58]. We simulate chromosome 10 of human GM12878 cell at 50 kb resolution ($N = 2712$) using Eq. (1), where the passive forces $-\nabla U$ originate from the MiChroM potential (see Appendix C and Fig. 11). Additionally, we introduce seven active loci (five in B compartments and two in A compartments) that model increased motor activity at those sites (Appendix C). We then study how the structural ensembles change when the active loci correspond to three distinct regimes: passive ($F = 0$), active with short mean persistent path ($F = 5,\ \tau = 1$), and active with long mean persistent path ($F = 3,\ \tau = 30$) (Fig. 4).

2. *Localized activity may expand compact passive compartments, induce compartment switching, and displace the active loci to chromosome periphery*

Active loci exhibit enhanced dynamics, and the resulting agitation perturbs the compact compartments harboring the active loci. Active agitation opens up the compartments, leading to a higher radius of gyration [Fig. 4(d)]. The simulated Hi-C maps show local loss of contacts [Figs. 4(a) and 4(b)]. Structural perturbation via active loci also reflects in a change in the principal eigenvector of the correlation matrix (EV1) [Figs. 4(a) and 4(b)].

Active loci with long mean persistent paths extend out of the compartment and tend to move towards the chromosome periphery [Figs. 4(c), 4(d), and 12]. This leads to a light stripe in the simulated contact map, as the peripherally located active loci have limited interaction with the rest of the chromosome [Fig. 4(b)]. Highly correlated activity may diminish the passive-compartment strength or altogether flip the compartment signature (EV1) at the active site [Figs. 4(a) and 4(b)]. The Hi-C signature resembles the "jetlike" protrusions observed in experiments at localized loading sites of loop extruders (SMC complexes) [86].

Activity with a long mean persistent time may arise from persistent bursts of transcription lasting for many seconds to minutes. Positioning of transcriptionally active segments

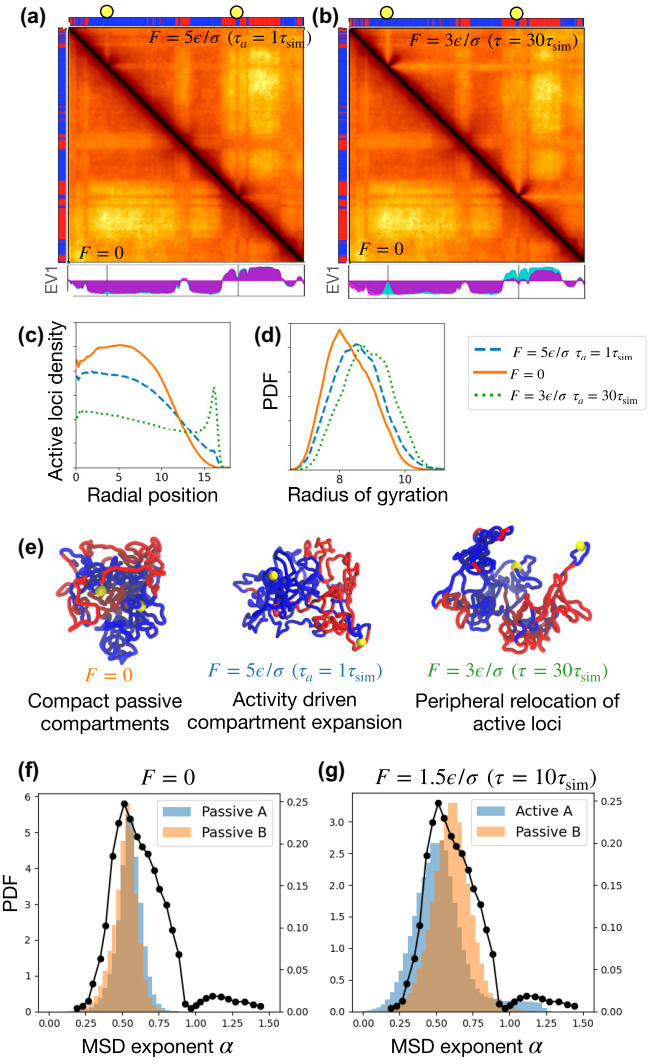

FIG. 4. Activity expands passive compartments and contributes to heterogeneity in dynamics. (a) Simulated contact maps showing a 30-Mb segment (50–80 Mb) of the GM12878 chromosome 10. The lower triangle corresponds to the passive structure ($F = 0$), while the upper triangle corresponds to the active steady state with $F = 5$ and $\tau = 1$. The thermal temperature is $k_BT = 1.0\epsilon$. (b) Same as (a) with activity corresponding to a longer mean persistent time $F = 3$ and $\tau = 30$. The bars on the top and left of the contact maps show the A- (red) and B- (blue) type beads that drive A/B compartments via passive phase separation. The yellow circles denote the two active sites in the segment. The principal eigenvectors (EV1) are shown in the subpanel below, where the passive (active) EV1 is colored in cyan (magenta). (c) Number density of active loci (including all the seven loci) plotted as a function of radial position (σ units). (d) Radius of gyration (σ units) of the 30-Mb segment plotted in the contact maps above. (e) Simulation snapshots of the 30-Mb segment containing two active loci shown as yellow spheres. The A-type (B-type) regions are shown in red (blue). (f) Distribution of MSD exponents α for chromosome 10 simulated with passive MiChroM ($F = 0$) measured over lag times 1–100τ_{sim}. (g) Same as (f) but with active A compartments ($F = 1.5\epsilon/\sigma,\ \tau = 10\tau_{sim}$). The black line with points (plotted on the right y axis) corresponds to experiments in human U2OS cells [35].

to the periphery of chromosome territories is experimentally well documented [15,59,87–90]. Additionally, high transcriptional activity is correlated with long genes looping out of the chromosome territories [59]. The peripheral positioning of highly expressed genes leads to loss of contact with the rest of the chromosome, which has also been observed recently [91]. Activating transcription within a repressive compartment may drive compartment switching, which may ultimately lead to cell-fate transitions [12,82]. The active model argues that the motorized mechanics of the transcription process directly contribute to all these phenomena. Modeling motor activity as higher temperature also shows the structural relocation of active monomers to the periphery [45,92], which may be compared with the low correlation time activity [Figs. 4(a) and 4(c)]. However, the effect is stronger for activity with higher correlation times [Figs. 4(b) and 4(c)].

3. *Activity increases the heterogeneity in chromatin dynamics*

Passive MiChroM is useful for reconstructing the structure from Hi-C maps, but the heterogeneity in chromatin dynamics is somewhat underrepresented [Fig. 4(f)]. In fact, any passive model is incapable of recapitulating superdiffusive chromatin loci, represented by $\alpha > 1$ in experimental data [Figs. 4(f) and 4(g)] [35,39]. Adding activity to the A compartments of passive MiChroM leads to a substantial widening of the MSD exponent distribution, better recapitulating the experimental observations [Fig. 4(g)]. Active simulations also exhibit the superdiffusive fraction, which is a feature of the active A compartments. Our model suggests that motor-driven active forces are an essential component in modeling the dynamics of chromosomes. While an important aspect of chromosome dynamics is derived just from its polymer nature, motor activity is the additional ingredient necessary to fully capture chromosome dynamics.

IV. DISCUSSION

We have studied a coarse-grained polymer model of chromosomes that, in addition to the uncorrelated thermal noise, experiences a temporally correlated active noise [Eqs. (1) and (2)]. This active noise models the effect of microscopic motors exerting forces inside the coarse-grained monomer (Fig. 1). Being internal, these forces must be balanced, with no net forces on the center of mass. At the molecular scale, one can think of such activity as pointlike dipolar forces. We only consider network degrees of freedom in our model and not fluid stress propagation. In such an overdamped Brownian dynamics model, forces must balance within the network. This balance, however, may only occur at scales of the order of the distance between entanglements or points of contact between non-neighboring segments in the network. Moreover, at such entanglement points, forces can branch, resulting in more complex multipolar forces on coarse-grained scales, although with still vanishing net force on the center of mass. Thus, although the presented model allows for unbalanced active force at each monomer, the model does ensure that the net force on larger network scales is balanced, due to the large number of randomly oriented active force monopoles. Hence, there is no net momentum of the polymer center of mass in our model. We additionally verified the momentum conservation of the polymer network by implementing a variation of the model where the active noise of each monomer is modified such that the polymer center of mass is suppressed (Figs. 13–15). All the qualities of our results remain unchanged except for an enhanced suppression of the apparent diffusion constant of the center of mass of the active polymer in certain regimes.

We have presented a simplified characterization of the steady state of the active polymer using two parameters: the force F depicting the active noise amplitude and the correlation time τ controlling the temporal persistence of the active noise [Figs. 2(a) and 3(b)]. The model exhibits diverse structural and dynamic properties. Active-polymer dynamics span subdiffusion, effective diffusion, and superdiffusion, where the correlated active kicks underlie the superdiffusive regime [Figs. 2(f) and 3(f)]. Importantly, nonequilibrium activity can result not only in enhanced monomer dynamics (e.g., superdiffusion) but also in structure formation that arises from stochastic active forces. Contrasting features like polymer swelling/collapse and radial phase segregation with higher monomer density towards the center/periphery are some of the actively controlled structural aspects [Figs. 2(b)–2(d) and 3(c)–3(e)]. The active steady-state structures may look similar to that of a passive system with attractive or repulsive interactions between monomers; however, the underlying mechanisms are completely different [Figs. 2(d) and 3(e)], i.e., the dynamics is essential to distinguish between active and passive mechanisms.

We proposed motor-driven collapse as a mechanism of chromosome compartmentalization. These compartments are steric hindrance and entanglement driven such that they can be destabilized via enzymes like type-II DNA topoisomerases that release entanglements. Upon entanglement release, the segments with correlated activity, such as highly transcribed genes, move toward the periphery of chromosomes. This posits that the motorized mechanics of transcription may be contributing to the relocation of the highly transcribed genes to chromosome territory edges. We also found that phase-separated compartments established by passive attractive forces are destabilized by activity due to the enhanced local dynamics (Fig. 4). Recent modeling has proposed that activity correlated along the polymer chain may drive compartmentalization [48]. Our model shows that compartmentlike compaction can also arise from an interplay of entanglements and temporally correlated activity. As mentioned before, the distinction between the active and passive mechanisms can be made based on measurements of dynamics [48].

Cell-type-specific variations in the genome architecture are reflected in the compartment structure [12,81–83]. These observations posit a conundrum: Do compartments drive gene expression or vice versa? While it is conceivable that the distinct chemical microenvironments within compartments help recruit transcription machinery thus aiding gene expression, our results suggest there is a possible mechanical feedback wherein a highly transcribed locus may alter the compartment structure surrounding the locus. Investigating the causality between compartments and gene expression is key to deciphering the genome structure-to-function relationship.

Chromatin loci typically show subdiffusion, which may be either passive or active in nature [28–31,93,94].

Interestingly, experiments have confirmed the presence of a wide distribution of dynamic exponents, including superdiffusion [35,38,39], which must be active in nature. We found that the passive chromosome model better recapitulated dynamic exponents when motor activity was added to the A compartments [Fig. 4(g)], suggesting motor activity as a driver of heterogeneity in dynamics. However, activity perturbed the structure to worsen agreement with Hi-C maps. This necessitates that the passive interactions be recalibrated in the presence of dynamics-satisfying motor activity, which is left for future work.

Our work is motivated in part by a large body of prior work on nonequilibrium aspects of cytoskeletal networks driven by molecular motor activity [1–3,62,64,67,70,95]. Persistent active noise has been argued to effectively capture stochastic binding and force generation by microscopic motors in polymer networks, giving rise to organization, mechanics, and dynamics on various timescales [64,67]. Models based on explicit motor-induced correlated forces upon stochastic binding have also been shown to recapitulate network contractility [3]. The present work builds on the prior approaches without explicit motor binding dynamics, where the motor binding/unbinding timescale is effectively captured by the active correlation time.

More recently, attention has turned to similar active matter aspects in chromosomes [40–43,45,46,48,49,66,96]. One class of active polymers corresponds to models with multiple temperatures. In this approach, monomers experience instantaneous thermal kicks, but there are at least two different types of monomers based on their effective temperature, i.e., "hot" and "cold" particles [45–47,77,92,97]. These models show structural features such as phase segregation, polymer enrichment at confinement boundaries, and dynamics aspects like a broad apparent diffusivity. However, the possibility of a superdiffusive dynamic regime is beyond such an approach.

Active polymer models that explicitly model active force dipoles constitute the second class of active models [49,98]. These models, utilizing instantaneous force dipoles, have shown a paradigm of structure and dynamics regulation by the dipolar strength. However, the dynamics lacks any superdiffusive component as well. Important contributions have been made by studies incorporating hydrodynamic aspects along with dipolar activity that argue active stresses originating from the dipoles as the driver of convective flows in the chromatin [96,99].

The treatment of activity as a temporally persistent noise, as done in the present work, has been explored in other models of flexible Rouse-like polymers [41,43,72]. These models explain the origin of a superdiffusive dynamics component due to the active correlation time, where a longer correlation time, resembling longer motor-residence times, drives a more prominent superdiffusive regime. This agrees with the explicit modeling of stochastic binding and force generation between motors and polymers, which shows an enhanced superdiffusive regime with higher motor concentrations and longer motor-residence times [42]. The present work, however, goes beyond dynamics and has identified for the first time an entangled-globule organization reminiscent of MIPS due to the combination of activity and repulsive interactions missing in prior Rouse-based models. One prior work [100] has studied self-avoidance and correlated active noise together in polymers but did not identify the novel structural and dynamic phases emerging in various activity regimes presented here, including the entangled-globule phase.

Through mechanistic explanations of various active steady states, the present work puts into perspective the observations of previous works like multiple-temperature activity as a special case of high force and low correlation time and thus widens the scope of possible structure and dynamic features of polymers driven by persistent activity. We hope this work will lead to many new nonequilibrium models of chromosomes and aid in the design of future experiments investigating the signatures of motor activity in chromosomes.

ACKNOWLEDGMENTS

This work was supported by the Center for Theoretical Biological Physics (CTBP) sponsored by the National Science Foundation (Grants No. PHY-2019745, No. PHY-2210291, and No. DMR-2224030) and by the Welch Foundation (Grant No. C-1792). We are grateful for the computational resources provided by Advanced Micro Devices. T.M. acknowledges funding from the Israel Science Foundation (Grant No. 1356/22). S.B. acknowledges the Robert A. Welch Postdoctoral Fellow program. We would like to thank Peter Wolynes, Vinicius G. Contessoto, Antonio Oliveira, Jr., and other members of CTBP for helpful discussions.

APPENDIX A: METHODS

1. Equation of motion

The overdamped equation of motion for the nth monomer is given by Eq. (1). The active force $f_n(t)$ denotes the temporally correlated active noise. The temporal evolution of the active force for the nth monomer is given as

$$\tau \frac{\partial f_n}{\partial t} = -f_n(t) + \sqrt{2\gamma\theta_a}\eta_n(t). \tag{A1}$$

Here τ is the correlation time of the active force and $\theta_a \equiv F^2\tau/\gamma$ is the temperaturelike quantity associated with activity. The amplitude of the active noise is denoted by F. Finally, $\eta_n(t)$ is a δ-correlated stationary Gaussian process with zero mean $\langle\eta(t)\rangle = 0$ and $\langle\eta_n(t)\eta_m(t')\rangle = \delta(t-t')\delta_{mn}$.

Solving the equation of motion of the active force [Eq. (A1)], we get the autocorrelation

$$\langle f_n(t) f_m(t')\rangle = F^2 e^{-(|t-t'|/\tau)}\delta_{mn}. \tag{A2}$$

The active force between different monomers is always uncorrelated. At short lag times $t \lesssim \tau$ the motor-induced noise for a monomer is correlated, leading to persistent dynamics, while at longer lag times $t \gg \tau$, the correlation vanishes exponentially.

2. Brownian dynamics simulations

We use Brownian dynamics simulations where the positions are updated at each time step based on forces and positions of the previous time step. We integrate the overdamped Langevin equation of motion of a monomer [Eq. (1)] using the following two steps.

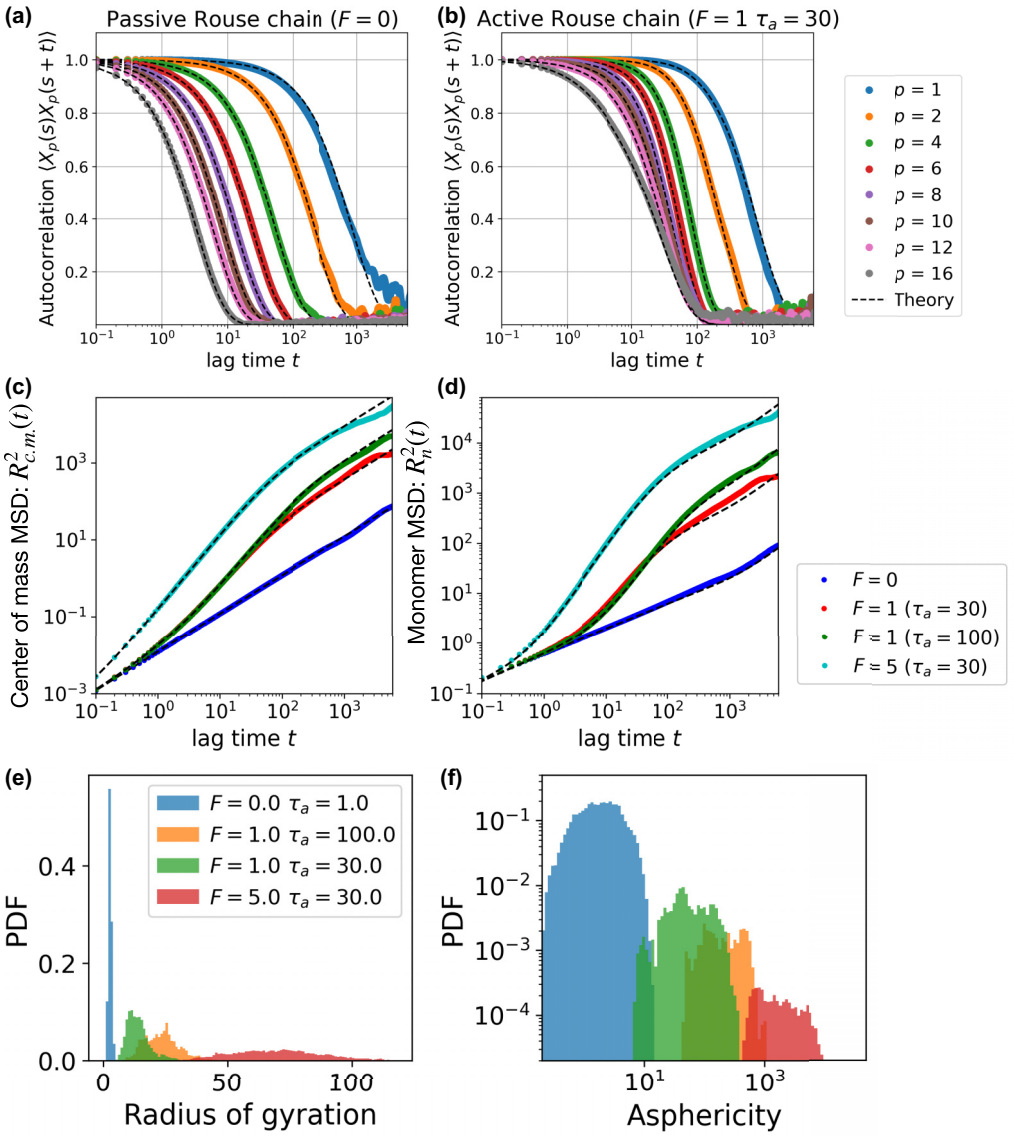

FIG. 5. Free Rouse chain. Rouse chain of size $N = 500$ and spring constant $k = 30\epsilon/\sigma^2$ simulated at $k_BT = 1$. Autocorrelation of Rouse modes for (a) passive and (b) active chains. The different colors represent different wave modes as shown in the legend. Note that for active chains the modes that relax at times longer than the correlation time $\tau = 30$ show equilibriumlike behavior, while the modes with characteristic relaxation time smaller than the correlation time have a prolonged relaxation under the active noise. The dashed lines show analytical results from Eq. (B3). Mean-square displacements for (c) center-of-mass motion and (d) monomer motion for Rouse chains. The longest Rouse relaxation time for this polymer is $\tau_1 \approx 850$. The dashed lines show theoretical expectations from Eqs. (B4) and (B5). (e) Radius of gyration of Rouse polymer for various values of F and τ. Increasing activity θ_a leads to a higher radius of gyration. (f) Distributions of asphericity of the polymer configurations, derived from the eigenvalues of the gyration tensor, show anisotropic and spheroidal structures with increasing activity.

(i) Compute the net force. Active forces at time t are computed from Eq. (A1),

$$f_n(t) = f_n(t - dt)e^{-dt/\tau} + F\sqrt{1 - e^{-2dt/\tau}}\mathcal{N}(0, 1), \quad \text{(A3)}$$

where $\mathcal{N}(0, 1)$ is a random variable drawn from a normal distribution with zero mean and unit standard deviation. Note that the active force does not depend on particle positions.

The net force $h_n(t)$ also has a passive contribution. The passive force is computed from the interaction potential using monomer positions $\{x(t)\}$:

$$h_n(t) = -\frac{\partial}{\partial x}\sum_m U[|x_n(t) - x_m(t)|] + f_n(t). \quad \text{(A4)}$$

(ii) Update positions. Then the monomer positions at time $t + dt$ are obtained according to Eq. (1):

$$x_n(t + dt) = x_n(t) + \frac{h_n(t)}{\gamma}dt + \sqrt{\frac{2T}{\gamma}dt}\mathcal{N}(0, 1). \quad \text{(A5)}$$

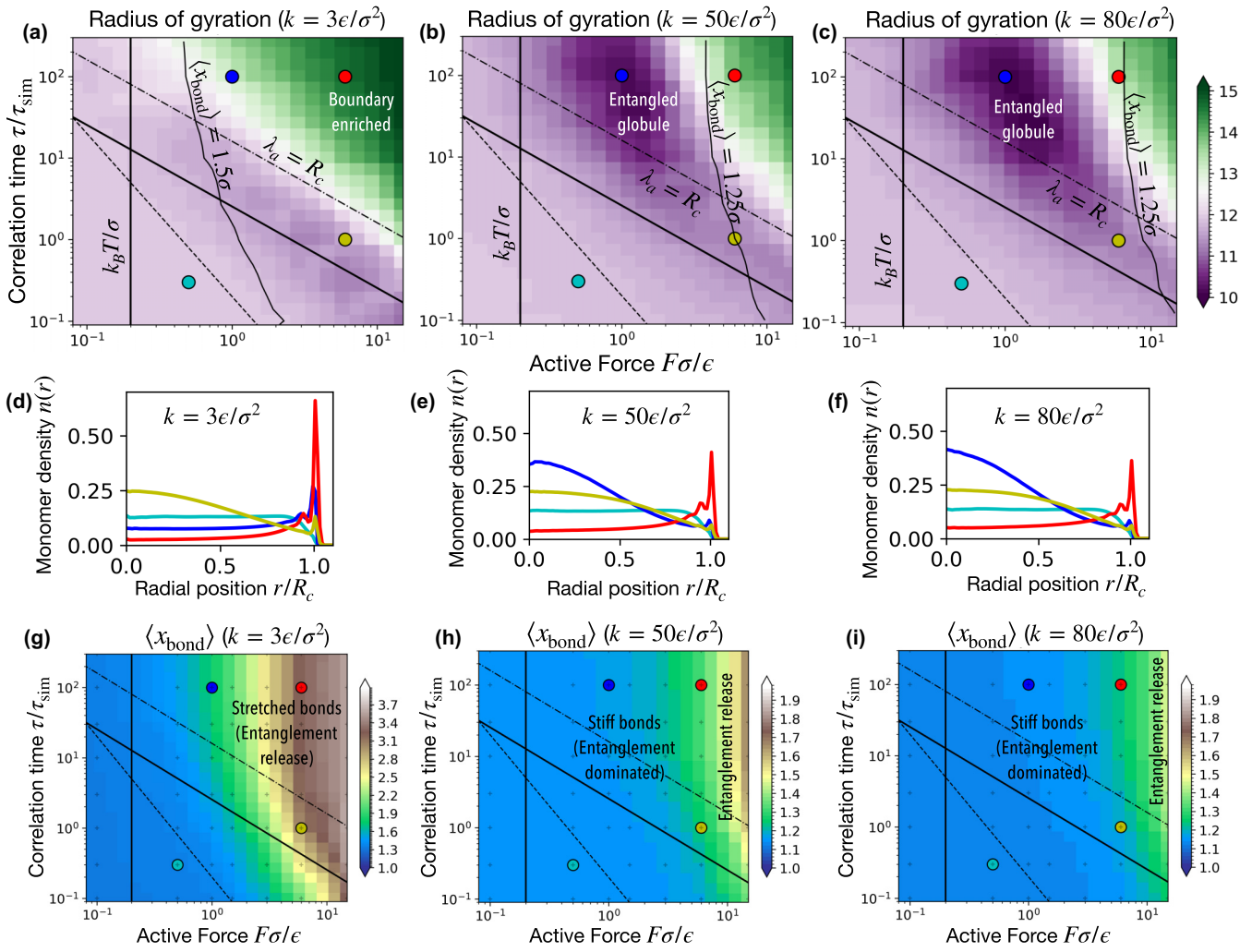

FIG. 6. Effect of spring constant on the entangled globule state. Self-avoiding polymer of size $N = 2000$ in spherical confinement with radius $R_0 = 16\sigma$ with various values of the spring constant k. (a)–(c) Active regime diagrams plotting the radius of gyration show the enhanced stability of the entangled-globule state for higher spring constants k. Note the shift of the mean bond length line $\langle x_{\rm bond}\rangle = 1.25\sigma$ along with the boundary of the entangled globule. (d)–(f) Radial profile of monomer density for various spring constants. (g)–(i) Contour plot showing the average bond length as a function of active force and correlation time for various spring constants. When the bond length is higher than 1.25σ the topological constraints are diminished, leading to entanglement release and destabilization of the entangled-globule state.

We simulate the equation of motion for each particle [Eq. (1)] using a custom integrator within the OPENMICHROM simulation package [61], which is built on top of OPENMM [101].

3. Simulation and physical units

The unit of distance is set by the monomer diameter σ. The simulation unit of energy is ϵ such that forces are measured in ϵ/σ. The simulation unit of time is $\tau_{\rm sim}$. We use a drag coefficient of $\gamma = 1.0\epsilon\tau_{\rm sim}/\sigma^2$.

To calibrate with physical units, we use $\epsilon = k_BT$. The monomer diameter corresponding to about 50 kb chromatin is $\sigma \approx 100$ nm. The apparent diffusion constant can be written as $D_{\rm app} = k_BT/\gamma = \sigma^2/\tau_{\rm sim}$. This equated with the experimentally observed apparent diffusion constant 0.01 μm^2/s; we get $\tau_{\rm sim} \sim 1$ s.

A different approach to calibration is to use an apparent viscosity of the nucleoplasm. Using the viscosity of water $\eta = 0.001$ Pa s, which is definitely an underestimate, we can write the drag coefficient $\gamma = 6\pi\eta\sigma$. Equating this with the previously mentioned definition of γ, we get the underestimated value $\tau_{\rm sim} \sim 0.01$ s.

Combining both these approaches, we use an order of magnitude calibration $\tau_{\rm sim} = 0.1$ s.

4. Polymer potential

The polymer potential consists of two terms: bonding between nearest neighbors and a short-range intermonomer repulsion to simulate self-avoidance. The nearest neighbors along the polymer chain are bonded using a linear spring $U_{nn} = (k/2)(r-d)^2$, where k is the spring constant and d is the unperturbed bond length. We use $k = 30\epsilon/\sigma^2$ unless specified otherwise. Here ϵ is the reduced unit of energy. For Rouse chains we use $d = 0$, while for all others we set $d = 1\sigma$.

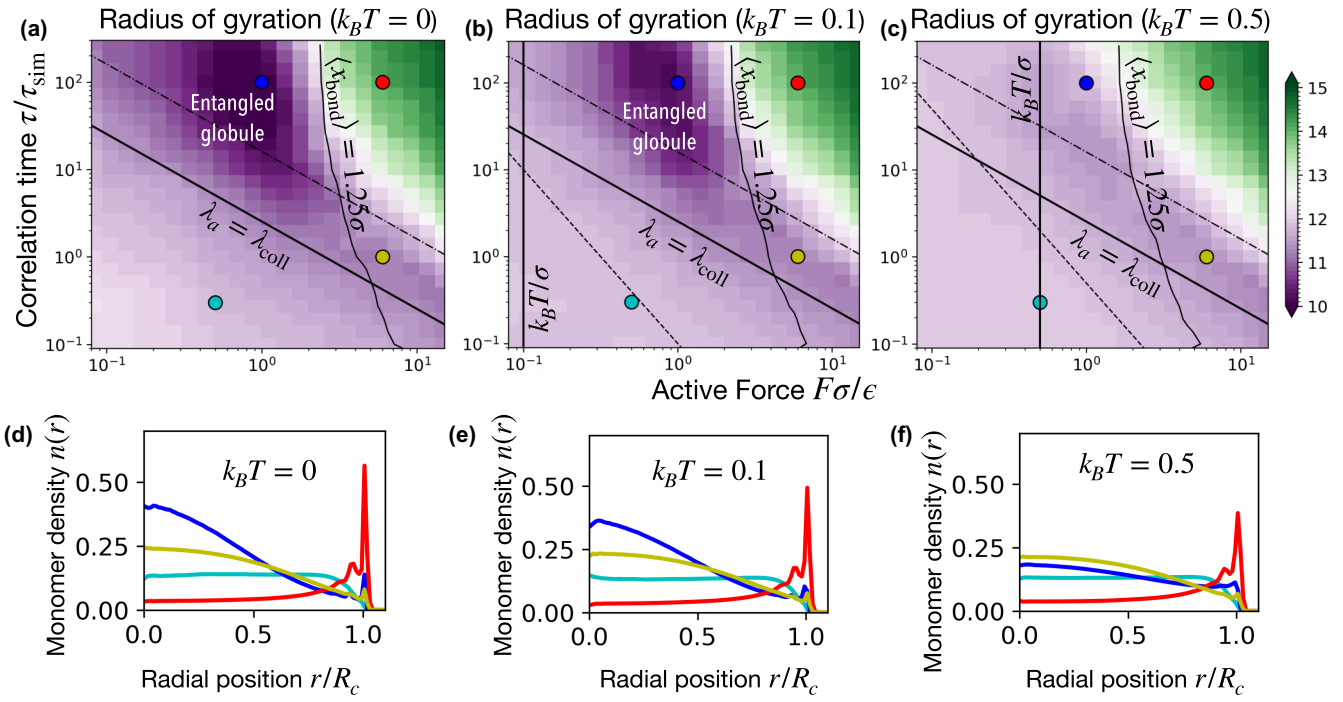

FIG. 7. Effect of temperature in destabilizing the entangled-globule state. Self-avoiding polymer of size $N = 2000$ in spherical confinement with radius $R_0 = 16\sigma$ simulated at various temperatures T. (a)–(c) Active regime diagrams plotting the radius of gyration show the enhanced stability of the entangled-globule state for lower temperatures. Note the shift of the thermal amplitude line k_BT/σ. (d)–(f) Radial profile of monomer density for various temperatures. When the thermal noise amplitude dominates the active noise $F < k_BT/\sigma$ the active correlations are destroyed and the entangled-globule state is destabilized.

Self-avoidance is modeled using a pairwise soft-core repulsive potential of the form $U_{sa}(r) = (E_0/2)\{1 + \tanh[1 - k_{sa}(r - d_{sa})]\}$, where $k_{sa} = 20\epsilon/\sigma^2$ encodes the steepness of the repulsion, $d_{sa} = 1\sigma$ is typical distance below which repulsion kicks in, and $E_0 = 5\epsilon$ is the maximum repulsive energy.

Finally, there is the spherical-confinement potential. We use a flat-bottom harmonic or half-harmonic restraint for the confinement $U_{conf} = (k_{conf}/2)(r - R_c)^2\Theta(r - R_c)$, where $\Theta(r - R_c)$ is the Heaviside Theta function that is zero when $r < R_c$ and one when $r \geqslant R_c$. We use $k_{conf} = 30\epsilon/\sigma^2$ throughout this work.

Chromosome potential. For the chromosome potential we utilize the optimized MiChroM parameters [19,61] to simulate the passive forces within our Brownian dynamics scheme [Eq. (1)]. We choose chromosome 10 of human GM12878 cell line, which has $N = 2711$ beads with each bead representing 50 kb DNA. The active loci are selected to be at the monomer indices 99, 376, 740, 1100, 1432, 1860, and 2340. We then study the effect on the passive structure as the activity is turned on for the active loci.

5. Simulation trajectory analysis

Starting from random configurations, the polymer is equilibrated at temperature T. We use $k_BT = 0.2\epsilon$ for simulations unless specified otherwise. Then activity with a fixed F and τ is turned on for every monomer, and simulations are run for 10^6 time steps with integration step $dt = 10^{-3}\tau_{sim}$ to establish the active steady state. We also use the analytical calculations of the Rouse polymer as a verification step for our simulations. Steady-state simulation for each parameter set is run for $10^4\tau_{sim}$, saving the particle coordinates every $0.1\tau_{sim}$. We simulate multiple replicas for each parameter for statistical analyses. All reported quantities, such as the radius of gyration, monomer density, and MSD, are computed from the steady-state trajectories. These quantities are also averaged over the ensemble.

a. Monomer density. The monomer density $n(r)$ is computed by counting the number of monomers in concentric shells such that $\int_0^{R_c} 4\pi r^2 n(r) dr = N$, where N is the total number of monomers.

b. Radial distribution function. The radial distribution function is computed from the standard definition $g(r) = dn_r\sigma^3/4\pi r^2 dr\phi$, where dn_r is the number of monomers within distance r and $r + dr$ from the center.

c. Displacement correlation between particles. The spatial correlation of displacements between particles was computed using the formula

$$C_x(\Delta r, \Delta t) = \left\langle \frac{1}{n} \sum_n \frac{\vec{d}_i(r, \Delta t) \cdot \vec{d}_j(r + \Delta r, \Delta t)}{\sqrt{d_i^2(r, \Delta t)\, d_j^2(r + \Delta r, \Delta t)}} \right\rangle,$$

where $d_i(r, \Delta t)$ is the displacement of the ith particle located at r over a lag time Δt and d_j is the corresponding displacement of the jth particle that is located a distance Δr away from the ith particle. The displacement correlation is summed over for all the n particles that lie within a sphere of radius Δr, and the angular brackets denote averaging over the trajectories.

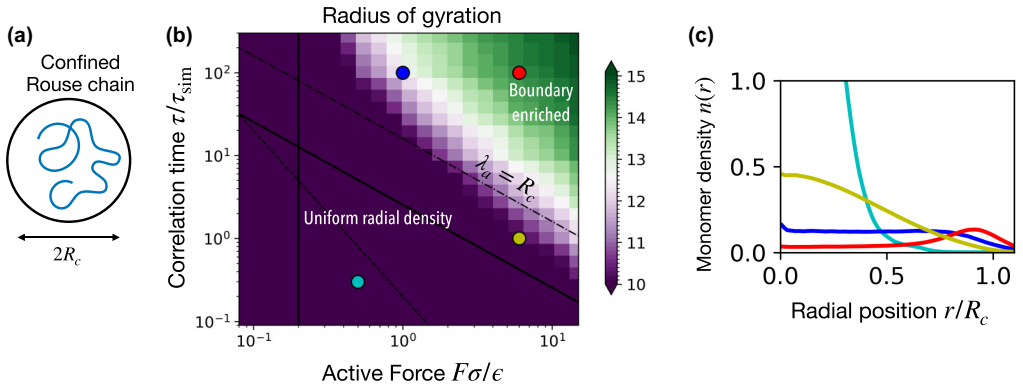

FIG. 8. Confined Rouse chain. (a) Rouse polymer of size $N = 2000$ in spherical confinement of size $R_0 = 16\sigma$. (b) Active regime diagram showing the radius of gyration as a function of the active force and correlation time. Boundary enrichment occurs when the mean persistent path λ_a exceeds the confinement dimension R_c. (c) Radial monomer density profile shows a monotonic decrease of density at the center with increasing activity, while the boundary becomes increasingly enriched.

d. Phase-separation coefficient. The phase-separation coefficient μ is defined as $\mu \equiv (\langle n_{AA}\rangle + \langle n_{PP}\rangle)/\langle 2n_{AP}\rangle$. Here n_{AA} is the number of pairwise contacts between A blocks (homotypic contacts), and n_{PP} (homotypic) and n_{AP} (heterotypic) are similarly defined. Two monomers are defined to be in contact when the distance between them is less than 1.5σ. Contacts between monomers of the same block are ignored to enhance the interblock phase-separation signal.

e. Active regime diagrams. Steady-state trajectories were generated for a logarithmically spaced grid with F varying between 0 and $15\epsilon/\sigma$ and τ varying between $0.1\tau_{\rm sim}$ and $300\tau_{\rm sim}$. The observables, like the radius of gyration, were computed for the above-mentioned grid and then interpolated into a finer grid to plot the active regime diagrams [Figs. 2(a) and 3(b)].

f. Contact maps. The contact maps were generated using the procedure described in Refs. [19,61]. The pairwise distance between monomers r_{ij} is converted to probability using the previously optimized sigmoid function $f_{\rm contact}(r_{ij}) = 0.5\{1 + \tanh[3.22(1.78 - r_{ij})]\}$ [19,61].

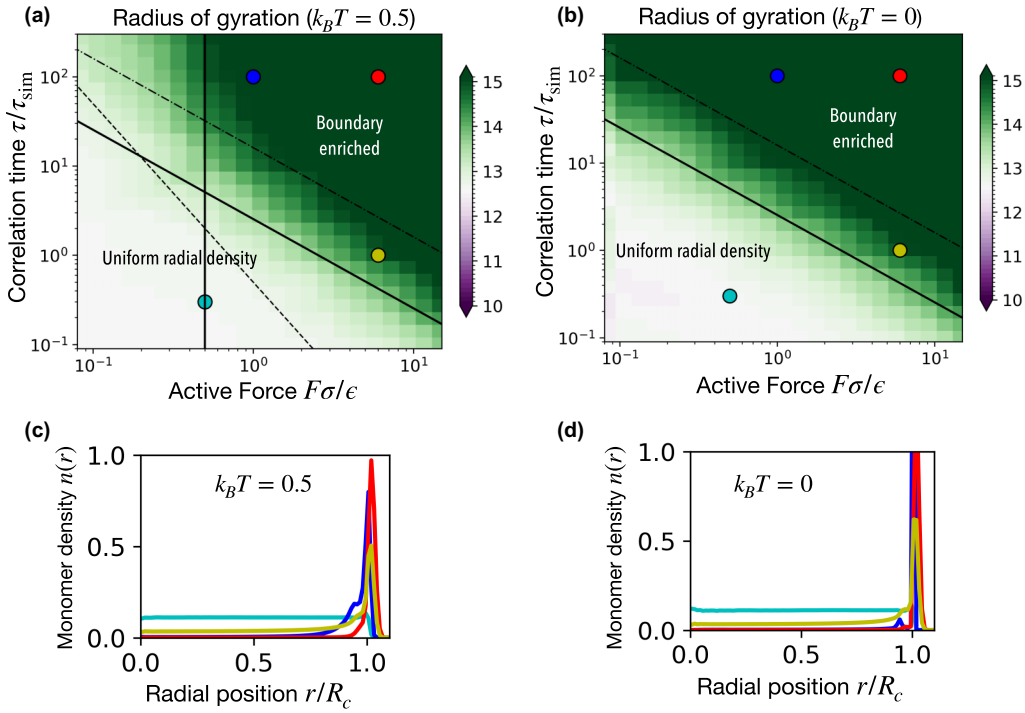

FIG. 9. Self-avoiding gas. Active regime diagram showing the radius of gyration of the gas particles as a function of the active force and the correlation time for $N = 2000$ self-avoiding active particles confined within a spherical cavity of radius $R_0 = 16\sigma$ simulated at two temperatures (a) $k_BT = 0.5$ and (b) $k_BT = 0$. There is a monotonic increase in the radius of gyration for high activity. (c) and (d) Monomer density $n(r)$ variation with the radial position. The boundary-enriched state may be observed when the mean persistent path is higher than the confinement dimension.

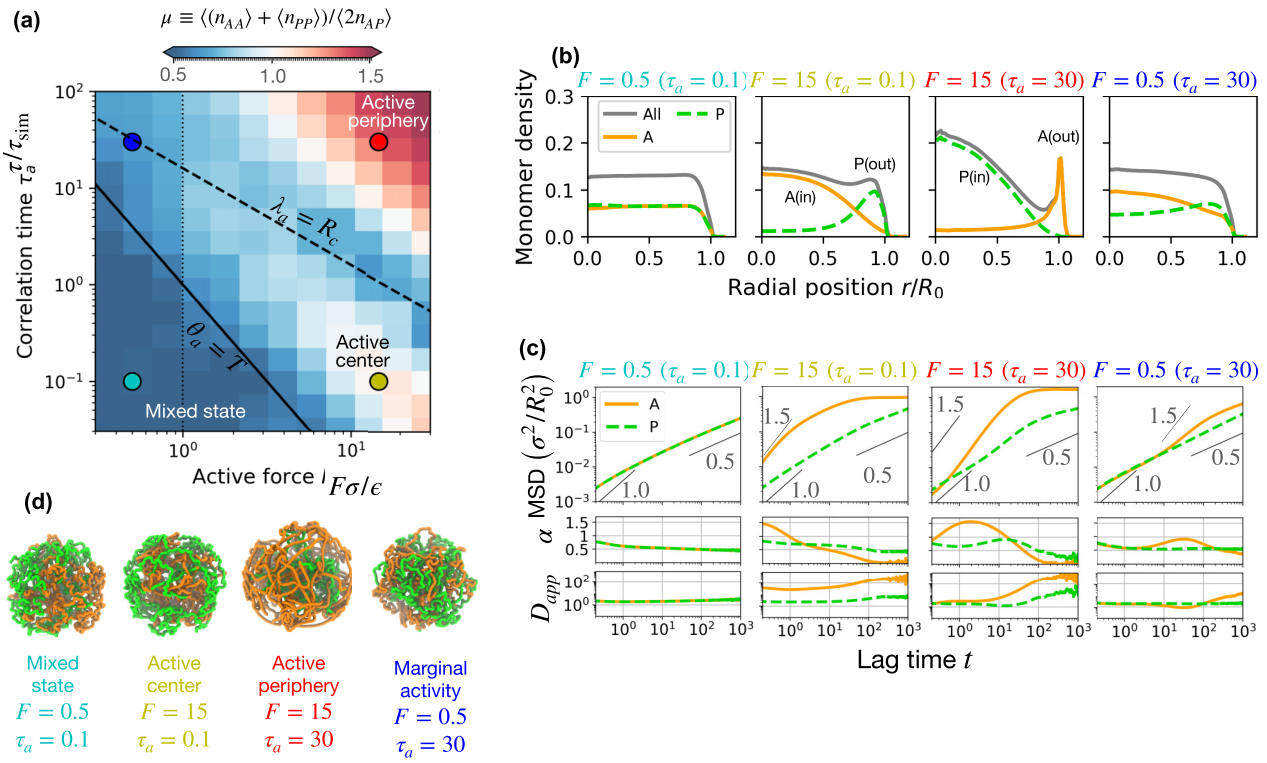

FIG. 10. Confined active-passive block copolymer at higher thermal temperature. (a) Active regime diagram of block copolymer in confinement at thermal temperature $k_BT = 1.0\epsilon$. Higher temperatures destabilize the entangled globule, leading to better segregation of active and passive blocks. Representative regions are selected on the F-τ phase space to show in the corresponding subfigures. (b) Radial monomer density of active and passive blocks showing radial segregation. (c) MSD versus lag time. The MSD exponent and apparent diffusivity are shown in subpanels. (d) Simulation snapshots of the block copolymer.

A tutorial on how to run the active simulations can be found in Ref. [102]. The simulation snapshots were generated using the Visual Molecular Dynamics software [103].

APPENDIX B: ACTIVE ROUSE POLYMER

Rouse chains, because of both their simplicity and analytical tractability, are a paradigm for studying polymer structure and dynamics. Considering a chain of N monomers, the equation of motion for the nth Rouse monomer reads [41,43]

$$\gamma \frac{\partial R_n}{\partial t} = k \frac{\partial^2 R_n}{\partial n^2} + f_n + \xi_n, \tag{B1}$$

where k is the spring constant associated with the harmonic bonds connecting the neighboring monomers.

1. Motor activity characterizes the relaxation spectrum of Rouse modes

Defining the pth normal mode of the Rouse chain, representing the dynamics in a subchain of size N/p, as

$$X_p(t) = \frac{1}{N}\int_0^N dn\, R_n(t)\cos(p\pi n/N), \tag{B2}$$

we obtain the autocorrelation between the Rouse modes for active chains [41]

$$\langle X_p(s)X_p(s+t)\rangle = \frac{\tau_p}{2N\gamma}\left(T + \frac{\theta_a}{1-\tau^2/\tau_p^2}\right)e^{-t/\tau_p} - \frac{\theta_a\tau}{2N\gamma\left(1-\tau^2/\tau_p^2\right)}e^{-t/\tau}, \tag{B3}$$

where $\tau_p = N^2\gamma/k\pi^2p^2$ is the equilibrium relaxation time of the pth mode. The longest Rouse relaxation time is given by $\tau_{\mathrm{Rse}} = N^2\gamma/k\pi^2$.

Figures 5(a) and 5(b) show the autocorrelation of Rouse modes of the active and passive chains from simulations and theory [Eq. (B3)]. The Rouse mode p with an equilibrium relaxation time τ_p that is longer than the active correlation time ($\tau_p \gg \tau$) appears equilibriumlike, i.e., the autocorrelation decays exponentially with a time constant approximately equal to τ_p [Fig. 5(b)]. However, activity raises the effective temperature associated with the modes to $T + \theta_a$. On the other hand, when the equilibrium relaxation time of the Rouse mode p is shorter than the activity persistent time ($\tau_p \ll \tau$), the mode autocorrelation relaxes exponentially with a time constant dominated by the active correlation time τ. This leads to crowding of the relaxation curves near the active correlation time in Fig. 5(b).

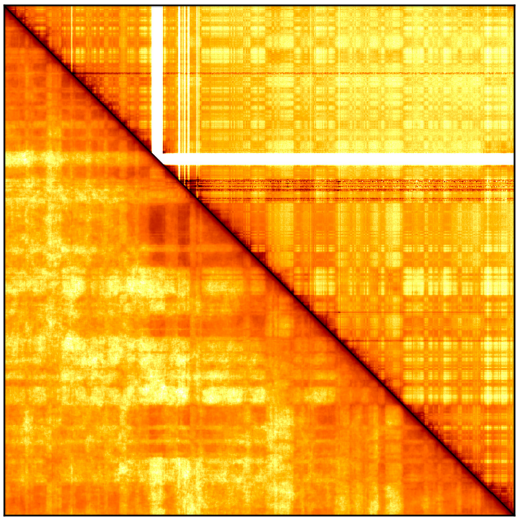

FIG. 11. Comparison with experiments. Comparing Hi-C maps from Rao *et al.* [13] with the base MiChroM model [19,61], obtained by setting activity to zero ($F = 0$) and $k_BT = 1.0\epsilon$. The upper triangle shows experimental data and the lower triangle is the simulation result for chromosome 10 of the human GM12878 cell line at 50 kb resolution.

2. Motor-induced persistent activity leads to diverse dynamic regimes

The scaling of MSD with time t, approximately t^α, defines the dynamic regime of the beads such as diffusion ($\alpha = 1$), subdiffusion ($\alpha < 1$), and superdiffusion ($\alpha > 1$), which includes ballistic motion ($\alpha = 2$). The MSD for the center-of-mass (c.m.) of a chain, governed by the zero-wave-number mode $R^2_{CM}(t) \equiv \langle (X_0(s+t) - X_0(s))^2 \rangle$, is given by

$$R^2_{\text{c.m.}}(t) = 2d\left(\frac{T+\theta_a}{N\gamma}t + \frac{\theta_a\tau}{N\gamma}\left(1 - e^{-t/\tau}\right)\right), \tag{B4}$$

where $d = 3$ is the dimension of space coordinates. The first term within large parentheses, proportional to t, is the diffusive term that dominates at long times $t \gg \tau$. Note that, at long times, the diffusion constantlike coefficient associated with the active polymer c.m. motion is $D_a^{\text{c.m.}} \equiv (T + \theta_a)/N\gamma$. Hence, at long times, the c.m. motion appears diffusive with an effective temperature $T + \theta_a$ and the expected drag coefficient of a Rouse polymer $N\gamma$. In contrast, at shorter times, there is a leading-order superdiffusive (ballistic) term (approximately t^2) that dominates thermal diffusion: $R^2_{\text{c.m.}}(t \ll \tau) \approx 2d(Tt/N\gamma + F^2t^2/N\gamma^2)$ [Fig. 5(c)].

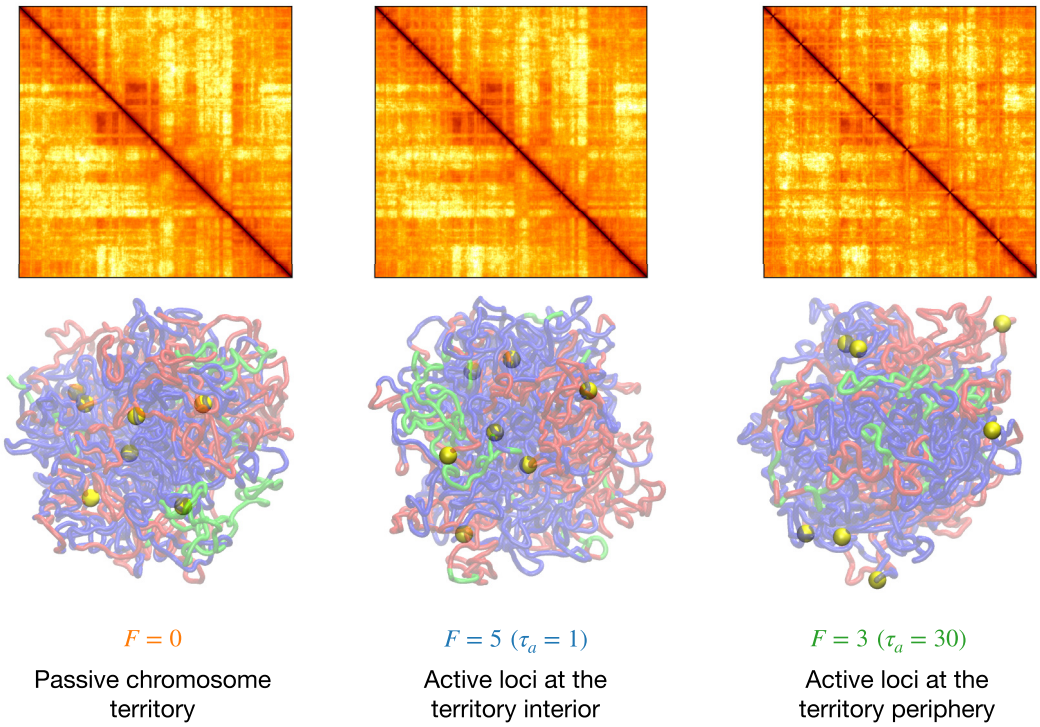

FIG. 12. Active perturbations to GM12878 chromosome 10. Simulation contact maps and snapshots of the GM12878 chromosome 10 for the passive and active cases. In the snapshots, *A*-type and *B*-type beads are colored in red and blue, respectively. In the active scenario, seven discrete loci, shown as yellow spheres, have active noise, while all the rest just have MiChroM potential. Active loci are more dynamic, which perturbs the compartments locally. Active loci with a long correlation time move to the periphery of the chromosome territory. The overall effect on the contact maps is minimal due to the low density of active loci, which only perturbs the effective-equilibrium structure locally.

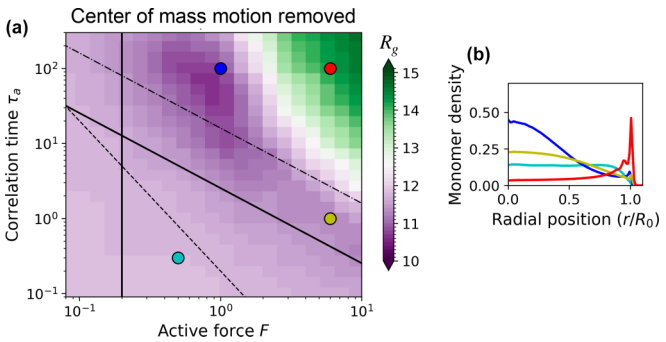

FIG. 13. Effect of the explicit center-of-mass motion correction on the active polymer regimes. (a) The radius of gyration of the active polymer for various active forces and correlation times is calculated in simulations where the active noise for each monomer is corrected so that the net center-of-mass motion is reduced. We implemented this using the CMMOTIONREMOVER scheme in OPENMM [101]. (b) Monomer radial density for the various regimes shown in (a). As can be noted by comparison with Figs. 2(a) and 2(b), the center-of-mass motion correction does not affect the active polymer regimes. This is a consequence of the active forces being balanced due to their random orientation (see Sec. IV).

On the other hand, the MSD for the nth monomer is given by a sum over all the Rouse modes p,

$$R_n^2(t) = R_{\text{c.m.}}^2(t) + 8d\sum_{p=1}^{\infty}\left[\frac{\tau_p}{2N\gamma}\left(T+\frac{\theta_a}{1-\tau^2/\tau_p^2}\right)\left(1-e^{-t/\tau_p}\right) - \frac{\theta_a\tau}{2N\gamma\left(1-\tau^2/\tau_p^2\right)}\left(1-e^{-t/\tau}\right)\right]\cos^2(p\pi n/N), \tag{B5}$$

where $R_{\text{c.m.}}^2(t)$ is defined in Eq. (B4) and $d=3$ is the space dimension. First, note that at very long times, when all the Rouse modes have relaxed ($t \gg \tau_p$ and $t \gg \tau$), monomer dynamics is governed by the c.m. motion, given by Eq. (B4). This transition occurs at lag times longer than the longest Rouse time τ_1 [Fig. 5(d)].

Interesting dynamic behaviors are observed at times comparable to the activity persistent time τ and τ_{Rse}. In the absence of activity, i.e., a passive system ($\theta_a = 0$), monomer MSD shows subdiffusion in the regime of lag times smaller than τ_{Rse}, while it shows diffusion corresponding to c.m. motion for lag times larger than τ_{Rse} (Fig. 5). For an active system, there is superdiffusive (near ballistic) signatures in the monomer MSD at times smaller than or comparable to the active persistent time τ. This is a direct consequence of correlated noise, which consistently propels the particles in a specific direction before changing the direction at lag times comparable to the persistent time. For lag times beyond the active persistent time but smaller than the Rouse time τ_{Rse}, the monomers move subdiffusively, albeit with a higher effective temperature (Fig. 5).

3. Motor activity drives swelling of Rouse polymer

Motor activity not only influences the dynamics, but it is consequential for the conformations as well. Motor-generated persistent forces stretch the polymer, leading to swollen conformations that exhibit a larger radius of gyration [Fig. 5(e)]. The temperaturelike quantity associated with activity $\theta_a \equiv F^2\tau/\gamma$; when it dominates the thermal temperature $T < \theta_a$, there is activity-driven swelling of the polymer. The swollen active polymers are spheroidal; asphericity increases with the active temperature θ_a [Fig. 5(f)].

4. Confined Rouse polymer

The Rouse chain in confinement does not show the structural regime corresponding to collapse at the center (Fig. 8). This is because self-avoidance is a necessary ingredient for center collapse. The monotonically increasing radius of

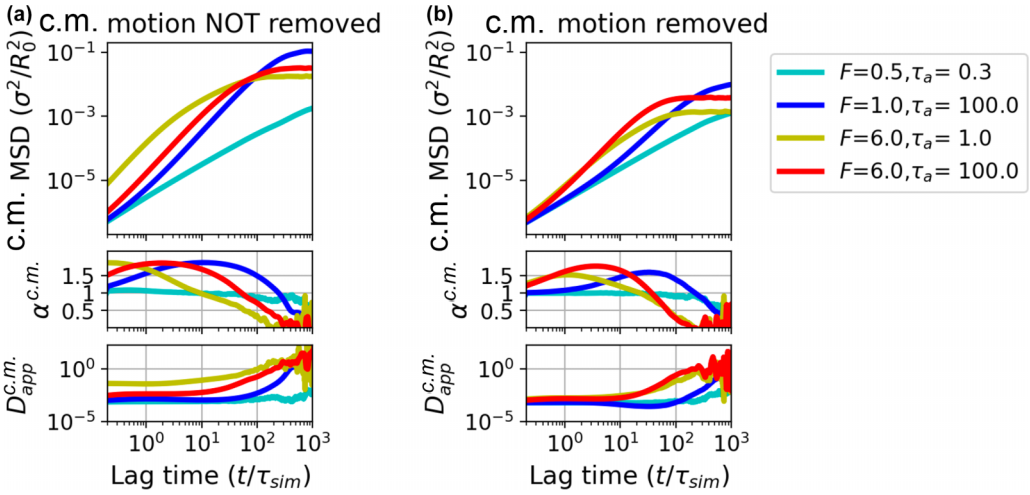

FIG. 14. Effect of the explicit center-of-mass motion correction on the center-of-mass mean-square displacement. (a) MSD of the center of mass (c.m.) of the active polymer without any motion correction for the center of mass. The subpanels show the apparent MSD exponent and the apparent diffusion constant. These simulations correspond to the ones shown in Fig. 2. (b) Same as in (a) but with c.m. motion correction implemented. Note, as expected, that the MSD and the apparent c.m. diffusion constant are suppressed upon c.m. motion removal.

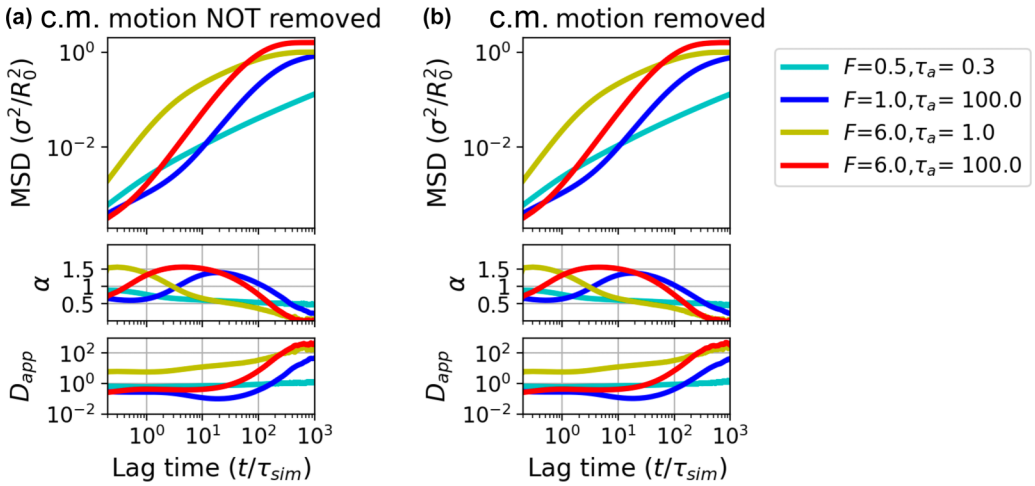

FIG. 15. Effect of the explicit center-of-mass motion correction on the monomer mean-square displacement. Average MSD of a monomer, the MSD exponent, and the apparent diffusion constant, (a) without and (b) with c.m. motion correction. (a) is the same as in Fig. 2(f). Note that the monomer MSDs are unchanged upon c.m. motion removal, which again is a direct consequence of the active forces already being balanced due to their random orientation (see Sec. IV).

gyration for Rouse polymers leads to only boundary enrichment when the mean persistent path is longer than the confinement dimension.

APPENDIX C: CHROMOSOME MODEL

We use the optimized MiChroM chromosome potential as described in Refs. [19,61] to simulate chromosome 10 of the human GM12878 lymphoblastoid cell using a 50 kb resolution model ($N = 2712$). MiChroM uses structural annotations to assign A- and B-type beads to the chromosome polymer and then the interaction profiles between the monomer types lead to the plaidlike patterns of interactions as seen in the Hi-C maps. There is an additional ideal chromosome term that drives lengthwise compaction or crumpling of the polymer along the contour, which is a feature of SMC-driven compaction. The simulated MiChroM contact maps and the corresponding experimental Hi-C maps [13] are shown in Fig. 11.

We added seven active loci along the chromosome at monomer indices 99, 376, 740, 1100, 1432, 1860, and 2340 and varied the activity in those loci to observe the corresponding change in the structure. The contact maps and representative structures for the passive case ($F = 0$) and active steady state with ($F = 3, \tau = 30$) and ($F = 5, \tau = 1$), simulated at $k_BT = 1$, are shown in Fig. 12. Long correlation times representing persistent transcription activity drive the active loci to the periphery of chromosome territories.

[1] D. Mizuno, C. Tardin, C. F. Schmidt, and F. C. MacKintosh, Nonequilibrium mechanics of active cytoskeletal networks, Science **315**, 370 (2007).

[2] P. M. Bendix, G. H. Koenderink, D. Cuvelier, Z. Dogic, B. N. Koeleman, W. M. Brieher, C. M. Field, L. Mahadevan, and D. A. Weitz, A quantitative analysis of contractility in active cytoskeletal protein networks, Biophys. J. **94**, 3126 (2008).

[3] S. Wang and P. G. Wolynes, Active contractility in actomyosin networks, Proc. Natl. Acad. Sci. USA **109**, 6446 (2012).

[4] S. Wang and P. G. Wolynes, On the spontaneous collective motion of active matter, Proc. Natl. Acad. Sci. USA **108**, 15184 (2011).

[5] E. Tjhung, D. Marenduzzo, and M. E. Cates, Spontaneous symmetry breaking in active droplets provides a generic route to motility, Proc. Natl. Acad. Sci. USA **109**, 12381 (2012).

[6] L. Blanchoin, R. Boujemaa-Paterski, C. Sykes, and J. Plastino, Actin dynamics, architecture, and mechanics in cell motility, Physiol. Rev. **94**, 235 (2014).

[7] V. Hakim and P. Silberzan, Collective cell migration: A physics perspective, Rep. Prog. Phys. **80**, 076601 (2017).

[8] T. Cremer and C. Cremer, Chromosome territories, nuclear architecture and gene regulation in mammalian cells, Nat. Rev. Genet. **2**, 292 (2001).

[9] W. A. Bickmore, The spatial organization of the human genome, Annu. Rev. Genom. Hum. G. **14**, 67 (2013).

[10] C. Hoencamp, O. Dudchenko, A. M. Elbatsh, S. Brahmachari *et al.*, 3D genomics across the tree of life reveals condensin II as a determinant of architecture type, Science **372**, 984 (2021).

[11] E. Lieberman-Aiden, N. L. V. Berkum, L. Williams, M. Imakaev, T. Ragoczy, A. Telling, I. Amit, B. R. Lajoie, P. J. Sabo, M. O. Dorschner, R. Sandstrom, B. Bernstein, M. A. Bender, M. Groudine, A. Gnirke, J. Stamatoyannopoulos, and L. A. Mirny, Comprehensive mapping of long-range interactions reveals folding principles of the human genome, Science **326**, 289 (2009).

[12] J. R. Dixon, I. Jung, S. Selvaraj, Y. Shen, J. E. Antosiewicz-Bourget, A. Y. Lee, Z. Ye, A. Kim, N. Rajagopal, W. Xie, Y. Diao, J. Liang, H. Zhao, V. V. Lobanenkov, J. R. Ecker, J. A. Thomson, and B. Ren, Chromatin architecture reorganization during stem cell differentiation, Nature (London) **518**, 331 (2015).

[13] S. S. P. Rao, M. H. Huntley, N. C. Durand, E. K. Stamenova, I. D. Bochkov, J. T. Robinson, A. L. Sanborn, I. Machol, A. D. Omer, E. S. Lander, and E. Lieberman-Aiden, A 3D map of the human genome at kilobase resolution reveals principles of chromatin looping, Cell **159**, 1665 (2014).

[14] A. N. Boettiger, B. Bintu, J. R. Moffitt, S. Wang, B. J. Beliveau, G. Fudenberg, M. Imakaev, L. A. Mirny, C. T. Wu, and X. Zhuang, Super-resolution imaging reveals distinct chromatin folding for different epigenetic states, Nature (London) **529**, 418 (2016).

[15] B. Bintu, L. J. Mateo, J.-H. Su, N. A. Sinnott-Armstrong, M. Parker, S. Kinrot, K. Yamaya, A. N. Boettiger, and X. Zhuang, Super-resolution chromatin tracing reveals domains and cooperative interactions in single cells, Science **362**, eaau1783 (2018).

[16] E. M. Hildebrand and J. Dekker, Mechanisms and functions of chromosome compartmentalization, Trends Biochem. Sci. **45**, 385 (2020).

[17] J. H. Su, P. Zheng, S. S. Kinrot, B. Bintu, and X. Zhuang, Genome-scale imaging of the 3D organization and transcriptional activity of chromatin, Cell **182**, 1641 (2020).

[18] M. Falk, Y. Feodorova, N. Naumova, M. Imakaev, B. R. Lajoie, H. Leonhardt, B. Joffe, J. Dekker, G. Fudenberg, I. Solovei, and L. A. Mirny, Heterochromatin drives compartmentalization of inverted and conventional nuclei, Nature (London) **570**, 395 (2019).

[19] M. D. Pierro, B. Zhang, E. L. Aiden, P. G. Wolynes, and J. N. Onuchic, Transferable model for chromosome architecture, Proc. Natl. Acad. Sci. USA **113**, 12168 (2016).

[20] Y. Qi, A. Reyes, S. E. Johnstone, M. J. Aryee, B. E. Bernstein, and B. Zhang, Data-driven polymer model for mechanistic exploration of diploid genome organization, Biophys. J. **119**, 1905 (2020).

[21] A. Esposito, S. Bianco, A. M. Chiariello, A. Abraham, L. Fiorillo, M. Conte, R. Campanile, and M. Nicodemi, Polymer physics reveals a combinatorial code linking 3D chromatin architecture to 1D chromatin states, Cell Rep. **38**, 110601 (2022).

[22] H. Wong, H. Marie-Nelly, S. Herbert, P. Carrivain, H. Blanc, R. Koszul, E. Fabre, and C. Zimmer, A predictive computational model of the dynamic 3D interphase yeast nucleus, Curr. Biol. **22**, 1881 (2012).

[23] D. Jost, P. Carrivain, G. Cavalli, and C. Vaillant, Modeling epigenome folding: Formation and dynamics of topologically associated chromatin domains, Nucleic Acids Res. **42**, 9553 (2014).

[24] M. Chiang, D. Michieletto, C. A. Brackley, N. Rattanavirotkul, H. Mohammed, D. Marenduzzo, and T. Chandra, Polymer modeling predicts chromosome reorganization in senescence, Cell Rep. **28**, 3212 (2019).

[25] G. Shi and D. Thirumalai, From Hi-C contact map to three-dimensional organization of interphase human chromosomes, Phys. Rev. X **11**, 011051 (2021).

[26] Q. MacPherson, B. Beltran, and A. J. Spakowitz, Bottom–up modeling of chromatin segregation due to epigenetic modifications, Proc. Natl. Acad. Sci. USA **115**, 12739 (2018).

[27] S. Fujishiro and M. Sasai, Generation of dynamic three-dimensional genome structure through phase separation of chromatin, Proc. Natl. Acad. Sci. USA **119**, e2109838119 (2022).

[28] I. Bronstein, Y. Israel, E. Kepten, S. Mai, Y. Shav-Tal, E. Barkai, and Y. Garini, Transient anomalous diffusion of telomeres in the nucleus of mammalian cells, Phys. Rev. Lett. **103**, 018102 (2009).

[29] H. Hajjoul, J. Mathon, H. Ranchon, I. Goiffon, J. Mozziconacci, B. Albert, P. Carrivain, J. M. Victor, O. Gadal, K. Bystricky, and A. Bancaud, High-throughput chromatin motion tracking in living yeast reveals the flexibility of the fiber throughout the genome, Genome Res. **23**, 1829 (2013).

[30] A. Zidovska, D. A. Weitz, and T. J. Mitchison, Micron-scale coherence in interphase chromatin dynamics, Proc. Natl. Acad. Sci. USA **110**, 15555 (2013).

[31] S. C. Weber, A. J. Spakowitz, and J. A. Theriot, Nonthermal ATP-dependent fluctuations contribute to the *in vivo* motion of chromosomal loci, Proc. Natl. Acad. Sci. USA **109**, 7338 (2012).

[32] B. Gu, T. Swigut, A. Spencley, M. R. Bauer, M. Chung, T. Meyer, and J. Wysocka, Transcription-coupled changes in nuclear mobility of mammalian cis-regulatory elements, Science **359**, 1050 (2018).

[33] S. S. Ashwin, T. Nozaki, K. Maeshima, and M. Sasai, Organization of fast and slow chromatin revealed by single-nucleosome dynamics, Proc. Natl. Acad. Sci. USA **116**, 19939 (2019).

[34] H. Ma, L.-C. Tu, Y.-C. Chung, A. Naseri, D. Grunwald, S. Zhang, and T. Pederson, Cell cycle- and genomic distance-dependent dynamics of a discrete chromosomal region, J. Cell Biol. **218**, 1467 (2019).

[35] H. A. Shaban, R. Barth, L. Recoules, and K. Bystricky, Hi-D: Nanoscale mapping of nuclear dynamics in single living cells, Genome Biol. **21**, 95 (2020).

[36] J. Lerner, P. A. Gomez-Garcia, R. L. McCarthy, Z. Liu, M. Lakadamyali, and K. S. Zaret, Two-parameter mobility assessments discriminate diverse regulatory factor behaviors in chromatin, Mol. Cell **79**, 677 (2020).

[37] H. Salari, M. D. Stefano, and D. Jost, Spatial organization of chromosomes leads to heterogeneous chromatin motion and drives the liquid- or gel-like dynamical behavior of chromatin, Genome Res. **32**, 28 (2022).

[38] A. Javer, N. J. Kuwada, Z. Long, V. G. Benza, K. D. Dorfman, P. A. Wiggins, P. Cicuta, and M. C. Lagomarsino, Persistent super-diffusive motion of *Escherichia coli* chromosomal loci, Nat. Commun. **5**, 3854 (2014).

[39] I. Eshghi, J. A. Eaton, and A. Zidovska, Interphase chromatin undergoes a local sol-gel transition upon cell differentiation, Phys. Rev. Lett. **126**, 228101 (2021).

[40] A. Ghosh and N. Gov, Dynamics of active semiflexible polymers., Biophys. J. **107**, 1065 (2014).

[41] D. Osmanović and Y. Rabin, Dynamics of active Rouse chains, Soft Matter **13**, 963 (2017).

[42] M. Foglino, E. Locatelli, C. A. Brackley, D. Michieletto, C. N. Likos, and D. Marenduzzo, Non-equilibrium effects

of molecular motors on polymers, Soft Matter **15**, 5995 (2019).
[43] A. Ghosh and A. J. Spakowitz, Statistical behavior of nonequilibrium and living biological systems subjected to active and thermal fluctuations, Phys. Rev. E **105**, 014415 (2022).
[44] S. Singh and R. Granek, Active fractal networks with stochastic force monopoles and force dipoles unravel subdiffusion of chromosomal loci, arXiv:2307.12310.
[45] N. Ganai, S. Sengupta, and G. Menon, Chromosome positioning from activity-based segregation, Nucleic Acids Res. **42**, 4145 (2014).
[46] J. Smrek and K. Kremer, Small activity differences drive phase separation in active-passive polymer mixtures, Phys. Rev. Lett. **118**, 098002 (2017).
[47] I. Chubak, S. Pachong, K. Kremer, C. Likos, and J. Smrek, Active topological glass confined within a spherical cavity, Macromolecules **55**, 956 (2022).
[48] A. Goychuk, D. Kannan, A. K. Chakraborty, and M. Kardar, Polymer folding through active processes recreates features of genome organization, Proc. Natl. Acad. Sci. USA **120**, e2221726120 (2023).
[49] S. Shin, G. Shi, H. W. Cho, and D. Thirumalai, Transcription-induced active forces suppress chromatin motion, Proc. Natl. Acad. Sci. USA **121**, e2307309121 (2024).
[50] J. Gelles and R. Landick, Rna polymerase as a molecular motor, Cell **93**, 13 (1998).
[51] J. Ma, L. Bai, and M. D. Wang, Transcription under torsion, Science **340**, 1580 (2013).
[52] F. R. Neumann, V. Dion, L. R. Gehlen, M. Tsai-Pflugfelder, R. Schmid, A. Taddei, and S. M. Gasser, Targeted INO80 enhances subnuclear chromatin movement and ectopic homologous recombination, Genes Dev. **26**, 369 (2012).
[53] J. M. Kim, P. Visanpattanasin, V. Jou, S. Liu, X. Tang, Q. Zheng, K. Y. Li, J. Snedeker, L. D. Lavis, T. Lionnet, and C. Wu, Single-molecule imaging of chromatin remodelers reveals role of ATPase in promoting fast kinetics of target search and dissociation from chromatin, eLife **10**, e69387 (2021).
[54] M. Ganji, I. A. Shaltiel, S. Bisht, E. Kim, A. Kalichava, C. H. Haering, and C. Dekker, Real-time imaging of DNA loop extrusion by condensin, Science **360**, 102 (2018).
[55] S. Golfier, T. Quail, H. Kimura, and J. Brugués, Cohesin and condensin extrude DNA loops in a cell-cycle dependent manner, eLife **9**, e53885 (2020).
[56] M. E. Cates and J. Tailleur, Motility-induced phase separation, Annu. Rev. Condens. Matter Phys. **6**, 219 (2015).
[57] D. Martin, J. O'Byrne, M. E. Cates, É. Fodor, C. Nardini, J. Tailleur, and F. V. Wijland, Statistical mechanics of active Ornstein-Uhlenbeck particles, Phys. Rev. E **103**, 032607 (2021).
[58] S. Brahmachari, V. G. Contessoto, M. D. Pierro, and J. D. N. Onuchic, Shaping the genome via lengthwise compaction, phase separation, and lamina adhesion, Nucleic Acids Res. **50**, 4258 (2022).
[59] S. Leidescher, J. Ribisel, S. Ullrich, Y. Feodorova, E. Hildebrand, A. Galitsyna, S. Bultmann, S. Link, K. Thanisch, C. Mulholland, J. Dekker, H. Leonhardt, L. Mirny, and I. Solovei, Spatial organization of transcribed eukaryotic genes, Nat. Cell Biol. **24**, 327 (2022).
[60] G. Bajpai, D. Amiad Pavlov, D. Lorber, T. Volk, and S. Safran, Mesoscale phase separation of chromatin in the nucleus, eLife **10**, e63976 (2021).
[61] A. B. O. Junior, V. G. Contessoto, M. F. Mello, and J. N. Onuchic, A scalable computational approach for simulating complexes of multiple chromosomes, J. Mol. Biol. **433**, 166700 (2021).
[62] A. W. C. Lau, B. D. Hoffman, A. Davies, J. C. Crocker, and T. C. Lubensky, Microrheology, stress fluctuations, and active behavior of living cells, Phys. Rev. Lett. **91**, 198101 (2003).
[63] Y. Hatwalne, S. Ramaswamy, M. Rao, and R. A. Simha, Rheology of active-particle suspensions, Am. Phys. Soc. **92**, 118101 (2004).
[64] F. C. Mackintosh and A. J. Levine, Nonequilibrium mechanics and dynamics of motor-activated gels, Phys. Rev. Lett. **100**, 018104 (2008).
[65] M. C. Marchetti, J. F. Joanny, S. Ramaswamy, T. B. Liverpool, J. Prost, M. Rao, and R. A. Simha, Hydrodynamics of soft active matter, Rev. Mod. Phys. **85**, 1143 (2013).
[66] R. Bruinsma, A. Y. Grosberg, Y. Rabin, and A. Zidovska, Chromatin hydrodynamics, Biophys. J. **106**, 1871 (2014).
[67] A. Caspi, R. Granek, and M. Elbaum, Enhanced diffusion in active intracellular transport, Phys. Rev. Lett. **85**, 5655 (2000).
[68] T. Markovich, E. Tjhung, and M. E. Cates, Chiral active matter: microscopic 'torque dipoles' have more than one hydrodynamic description, New J. Phys. **21**, 112001 (2019).
[69] N. Fakhri, A. D. Wessel, C. Willms, M. Pasquali, D. R. Klopfenstein, F. C. MacKintosh, and C. F. Schmidt, High-resolution mapping of intracellular fluctuations using carbon nanotubes, Science **344**, 1031 (2014).
[70] M. Guo, A. J. Ehrlicher, M. H. Jensen, M. Renz, J. R. Moore, R. D. Goldman, J. Lippincott-Schwartz, F. C. Mackintosh, and D. A. Weitz, Probing the stochastic, motor-driven properties of the cytoplasm using force spectrum microscopy, Cell **158**, 822 (2014).
[71] C. Maggi, M. Paoluzzi, N. Pellicciotta, A. Lepore, L. Angelani, and R. D. Leonardo, Generalized energy equipartition in harmonic oscillators driven by active baths, Phys. Rev. Lett. **113**, 238303 (2014).
[72] A. Ghosh and A. J. Spakowitz, Active and thermal fluctuations in multi-scale polymer structure and dynamics, Soft Matter **18**, 6629 (2022).
[73] S. Brahmachari and J. F. Marko, Chromosome disentanglement driven via optimal compaction of loop-extruded brush structures, Proc. Natl. Acad. Sci. USA **116**, 24956 (2019).
[74] J. Stenhammar, D. Marenduzzo, R. J. Allen, and M. E. Cates, Phase behaviour of active Brownian particles: The role of dimensionality, Soft Matter **10**, 1489 (2014).
[75] R. G. Winkler and G. Gompper, The physics of active polymers and filaments, J. Chem. Phys. **153**, 040901 (2020).
[76] M. Doi and S. F. Edwards, *The Theory of Polymer Dynamics* (Clarendon Press, Oxford, 1988).
[77] J. Smrek, I. Chubak, C. N. Likos, and K. Kremer, Active topological glass, Nat. Commun. **11**, 26 (2020).
[78] Y. Cui and C. Bustamante, Pulling a single chromatin fiber reveals the forces that maintain its higher-order structure, Proc. Natl. Acad. Sci. USA **97**, 127 (2000).
[79] H. Yin, M. D. Wang, K. Svoboda, R. Landick, S. M. Block, and J. Gelles, Transcription against an applied force, Science **270**, 1653 (1995).

[80] B. T. Donovan, A. Huynh, D. A. Ball, H. P. Patel, M. G. Poirier, D. R. Larson, M. L. Ferguson, and T. L. Lenstra, Live-cell imaging reveals the interplay between transcription factors, nucleosomes, and bursting, EMBO J. **38**, e100809 (2019).

[81] D. Kurotaki, K. Kikuchi, K. Cui, W. Kawase, K. Saeki, J. Fukumoto, A. Nishiyama, K. Nagamune, K. Zhao, K. Ozato, P. P. Rocha, and T. Tamura, Chromatin structure undergoes global and local reorganization during murine dendritic cell development and activation, Proc. Natl. Acad. Sci. USA **119**, e2207009119 (2022).

[82] R. Vilarrasa-Blasi, P. Soler-Vila, N. Verdaguer-Dot, N. Russiñol, M. D. Stefano, V. Chapaprieta, G. Clot, I. Farabella, P. Cuscó, M. Kulis, X. Agirre, F. Prosper, R. Beekman, S. Beá, D. Colomer, H. G. Stunnenberg, I. Gut, E. Campo, M. A. Marti-Renom, and J. I. Martin-Subero, Dynamics of genome architecture and chromatin function during human B cell differentiation and neoplastic transformation, Nat. Commun. **12**, 651 (2021).

[83] B. Bonev, N. M. Cohen, Q. Szabo, L. Fritsch, G. L. Papadopoulos, Y. Lubling, X. Xu, X. Lv, J. P. Hugnot, A. Tanay, and G. Cavalli, Multiscale 3D genome rewiring during mouse neural development, Cell **171**, 557 (2017).

[84] D. Michieletto, M. Chiang, D. Colì, A. Papantonis, E. Orlandini, P. R. Cook, and D. Marenduzzo, Shaping epigenetic memory via genomic bookmarking, Nucleic Acids Res. **46**, 83 (2018).

[85] J. A. Owen, D. Osmanovic, and L. A. Mirny, Design principles of 3D epigenetic memory systems, Science **382**, eadg3053 (2023).

[86] Y. Guo, E. Al-Jibury, R. Garcia-Millan, K. Ntagiantas, J. W. King, A. J. Nash, N. Galjart, B. Lenhard, D. Rueckert, A. G. Fisher, G. Pruessner, and M. Merkenschlager, Chromatin jets define the properties of cohesin-driven *in vivo* loop extrusion, Mol. Cell **82**, 3769 (2022).

[87] N. L. Mahy, P. E. Perry, and W. A. Bickmore, Gene density and transcription influence the localization of chromatin outside of chromosome territories detectable by fish, J. Cell Biol. **159**, 753 (2002).

[88] T. Nagano, Y. Lubling, T. J. Stevens, S. Schoenfelder, E. Yaffe, W. Dean, E. D. Laue, A. Tanay, and P. Fraser, Single cell Hi-C reveals cell-to-cell variability in chromosome structure, Nature (London) **502**, 59 (2013).

[89] S. Chambeyron and W. A. Bickmore, Chromatin decondensation and nuclear reorganization of the *HoxB* locus upon induction of transcription, Genes Dev. **18**, 1119 (2004).

[90] R. R. Williams, S. Broad, D. Sheer, and J. Ragoussis, Subchromosomal positioning of the epidermal differentiation complex (EDC) in keratinocyte and lymphoblast interphase nuclei, Exp. Cell. Res. **272**, 163 (2002).

[91] W. Winick-Ng, A. Kukalev, I. Harabula, L. Zea-Redondo *et al.*, Cell-type specialization is encoded by specific chromatin topologies, Nature (London) **599**, 684 (2021).

[92] A. Agrawal, N. Ganai, S. Sengupta, and G. I. Menon, Nonequilibrium biophysical processes influence the large-scale architecture of the cell nucleus, Biophys. J. **118**, 2229 (2020).

[93] F. C. MacKintosh, Active diffusion: The erratic dance of chromosomal loci, Proc. Natl. Acad. Sci. USA **109**, 7138 (2012).

[94] K. Smith, B. Griffin, H. Byrd, F. C. Mackintosh, and M. L. Kilfoil, Nonthermal fluctuations of the mitotic spindle, Soft Matter **11**, 4396 (2015).

[95] T. Markovich, E. Tjhung, and M. E. Cates, Shear-induced first-order transition in polar liquid crystals, Phys. Rev. Lett. **122**, 088004 (2019).

[96] D. Saintillan, M. J. Shelley, and A. Zidovska, Extensile motor activity drives coherent motions in a model of interphase chromatin., Proc. Natl. Acad. Sci. USA **115**, 11442 (2018).

[97] P. Bera, A. Wasim, and J. Mondal, Hi-C embedded polymer model of *Escherichia coli* reveals the origin of heterogeneous subdiffusion in chromosomal loci, Phys. Rev. E **105**, 064402 (2022).

[98] S. Chaki, L. Theeyancheri, and R. Chakrabarti, A polymer chain with dipolar active forces in connection to spatial organization of chromatin, Soft Matter **19**, 1348 (2023).

[99] A. Mahajan, W. Yan, A. Zidovska, D. Saintillan, and M. J. Shelley, Euchromatin activity enhances segregation and compaction of heterochromatin in the cell nucleus, Phys. Rev. X **12**, 041033 (2022).

[100] Z. Jiang, Y. Qi, K. Kamat, and B. Zhang, Phase separation and correlated motions in motorized genome, J. Phys. Chem. B **126**, 5619 (2022).

[101] P. Eastman, J. Swails, J. D. Chodera, R. T. McGibbon, Y. Zhao, K. A. Beauchamp, L.-P. Wang, A. C. Simmonett, M. P. Harrigan, C. D. Stern, R. P. Wiewiora, B. R. Brooks, and V. S. Pande, OpenMM 7: Rapid development of high performance algorithms for molecular dynamics, PLoS Comput. Biol. **13**, e1005659 (2017).

[102] https://github.com/s-brahmachari/ActiveOpenMiChroM/tree/main/Tutorials/Active_Chromosome_Dynamics

[103] http://www.ks.uiuc.edu/Research/vmd/